

Article

# Comparison of Passive Microwave-Derived Early Melt Onset Records on Arctic Sea Ice

Angela C. Bliss <sup>1,2,\*</sup>, Jeffrey A. Miller <sup>1,3</sup> and Walter N. Meier <sup>1</sup>

<sup>1</sup> Cryospheric Sciences Laboratory, NASA Goddard Space Flight Center, Greenbelt, MD 20771, USA; jeffrey.a.miller@nasa.gov (J.A.M.); walt.meier@nasa.gov (W.N.M.)

<sup>2</sup> Earth System Science Interdisciplinary Center, University of Maryland, College Park, MD 20740, USA

<sup>3</sup> KBRwyle, Houston, TX 77058, USA

\* Correspondence: angela.c.bliss@nasa.gov; Tel.: +1-301-614-5037

Academic Editors: Xiaofeng Li and Prasad S. Thenkabail

Received: 23 November 2016; Accepted: 21 February 2017; Published: 24 February 2017

**Abstract:** Two long records of melt onset (MO) on Arctic sea ice from passive microwave brightness temperatures (Tbs) obtained by a series of satellite-borne instruments are compared. The Passive Microwave (PMW) method and Advanced Horizontal Range Algorithm (AHRA) detect the increase in emissivity that occurs when liquid water develops around snow grains at the onset of early melting on sea ice. The timing of MO on Arctic sea ice influences the amount of solar radiation absorbed by the ice–ocean system throughout the melt season by reducing surface albedos in the early spring. This work presents a thorough comparison of these two methods for the time series of MO dates from 1979 through 2012. The methods are first compared using the published data as a baseline comparison of the publically available data products. A second comparison is performed on adjusted MO dates we produced to remove known differences in inter-sensor calibration of Tbs and masking techniques used to develop the original MO date products. These adjustments result in a more consistent set of input Tbs for the algorithms. Tests of significance indicate that the trends in the time series of annual mean MO dates for the PMW and AHRA are statistically different for the majority of the Arctic Ocean including the Laptev, E. Siberian, Chukchi, Beaufort, and central Arctic regions with mean differences as large as 38.3 days in the Barents Sea. Trend agreement improves for our more consistent MO dates for nearly all regions. Mean differences remain large, primarily due to differing sensitivity of in-algorithm thresholds and larger uncertainties in thin-ice regions.

**Keywords:** Arctic; sea ice; melt; melt onset; passive microwave

## 1. Introduction

Satellite-based passive microwave observations have been used to monitor sea ice continuously since late 1978 [1], resulting in a long record of the annual growth and retreat cycle of Arctic sea ice consisting of multiple measures such as extent [2,3], melt season length [4,5], and sea ice season length [6]. During the spring and summer months, sea ice transitions from a cold, winter-like surface at the beginning of spring to the onset of melt and more advanced melting stages when melt ponds develop on the sea ice and sea ice extent retreats [7]. The spring transition period is known to be important for the annual surface energy budget of the Arctic. Modest reductions in surface albedo occur when melting begins [8] and liquid water develops between snow grains [9], thus contributing to increased absorption of solar radiation that enhances the ice–albedo feedback mechanism [10]. When coupled with increasing daylight hours in the spring, the timing of melt onset (MO) on Arctic sea ice can have a propagating effect through the remainder of the melt season [7]. Early melting on the sea ice reduces surface albedo earlier in the year, increasing the total amount of solar radiation absorbed

by the ice–ocean system throughout the melt season contributing to delayed autumn freeze-up and reduced wintertime ice growth [7].

The spatio-temporal patterns in MO timing on Arctic sea ice are largely controlled by spring weather systems [11,12]. The influence of enhanced cloud cover [8] and increased atmospheric moisture flux associated with the passage of cyclones result in increased downwelling longwave radiation and near-surface warming [13]. Prior to the day of MO, frontal systems from numerous cyclones precondition the snow and sea ice for melting through episodic warming of the air temperature at the inversion top and the upper portion of the snow–ice column [8]. Anomalous early MO at the regional scale can be associated with the presence of low-pressure systems, while high-pressure anomalies are associated with later regional melting [12].

Several algorithms to determine the timing of MO on the sea ice using passive microwave [5,14–16], active microwave [17–19], and combined methods [20–22] exist. The long length of the continuous record of passive microwave satellite observations makes it ideal for use in sea ice studies. Previous research using passive microwave based methods have documented the changes in regional trends of spring MO timing on Arctic sea ice over the satellite record [5,12,23,24]; however, no thorough comparison of long records of Arctic MO from passive microwave observations has been published thus far. A cursory comparison of two of these methods indicated considerable differences in regional trends of MO at the regional scale [23], warranting further investigation.

In this work, two long records of passive microwave MO dates on Arctic sea ice: the Advanced Horizontal Range Algorithm (AHRA) developed by Drobot and Anderson [15] and the Passive Microwave algorithm (hereafter PMW) developed by Markus et al. [5] are thoroughly compared. Statistical summaries of MO timing for Arctic sea ice over a 34-year overlap period (1979–2012) from the two methods are presented and the causes for existing differences are investigated. The primary research aims addressed here are (1) to compare the similarity of MO dates from the AHRA and PMW methods; (2) to document the major differences in the datasets and their limitations; and (3) to determine if agreement between the two MO algorithms can be improved by applying the AHRA and PMW methodology over passive microwave data from a single source dataset, thus testing how robust the MO algorithms are to differences in the pre-processing of source data. The results presented here can help inform data users of some of the primary differences between the MO datasets used for studies of Arctic sea ice and highlight the sensitivity of the algorithms to varied inter-sensor calibration corrections. The consistent application of inter-sensor calibration corrections over long multi-sensor data records used in this work can have implications for other passive microwave sea ice data products that rely on threshold values applied to corrected brightness temperatures.

## 2. Materials and Methods

The AHRA Snowmelt Onset on Arctic Sea Ice Version 3 MO dates [15] are distributed by the National Snow and Ice Data Center (NSIDC). The PMW Arctic Sea Ice Melt data are available from NASA Goddard Space Flight Center Cryospheric Sciences Research Portal (at <http://neptune.gsfc.nasa.gov/csb/index.php?section=54>, updated 2 July 2015) [5]. Both datasets use passive microwave brightness temperatures (Tbs) from a collection of several sensors: NASA's NIMBUS-7 Scanning Multichannel Microwave Radiometer (SMMR); a series of Special Sensor Microwave Imagers (SSM/I) onboard the Defense Meteorological Satellite Program's (DMSP) F8, F11, and F13 platforms; and the Special Sensor Microwave Imager and Sounder (SSMIS) onboard DMSP F17. The AHRA and PMW use gridded Tbs from the 19 GHz (18 GHz for SMMR data) and 37 GHz channels [5] on NSIDC's Northern Hemisphere polar stereographic grid [25]; the grid has a nominal spatial resolution of 25 km × 25 km, true at 70°N. SSM/I and SSMIS data are available daily. SMMR data for years 1979–1987 were collected every other day due to power limitations of the sensor [26], thus missing days are ignored by the MO algorithms. The AHRA and the early MO date from the PMW method are consistent with the “early melt” transition season defined by Livingstone et al. [27]. Table 1 summarizes some of the primary differences between the AHRA and PMW methodology. The AHRA and PMW methodology are

described briefly below. For full algorithm descriptions please see Drobot and Anderson [15] and Markus et al. [5].

**Table 1.** MO algorithm summary <sup>1</sup>.

	AHRA	PMW
<b>Algorithm starting day of year</b>	61 (2 March)	76 (17 March)
<b>Passive microwave channels</b>	19/18H and 37H GHz	19/18V and 37V GHz
<b>Melt criteria</b>	HR = Tb(19H) – Tb(37H)	$\Delta 37V =  Tb(37V)(i - 1) - Tb(37V)(i) $ ; $\Delta GR_{ice} = GR_{ice}(i) - GR_{ice}(i + 1)$ , where $GR_{ice} = (Tb_{ice}(37V) - Tb_{ice}(19V)) / (Tb_{ice}(37V) + Tb_{ice}(19V))$ ; $P = Tb(19V) + 0.8Tb(37V)$
<b>Time series testing method</b>	20-day window	Parameter weighting of melt criteria equations and neighborhood test for consistency
<b>Sea ice masking method</b>	50% sea ice concentration on one of first two days of March	Pixels with 80% sea ice concentration for at least 5 days of the year (NASA Team)

<sup>1</sup> For full algorithm details, please refer to Drobot and Anderson [15] and Markus et al. [5]. Passive microwave channels and melt criteria are described further in Sections 2.1 and 2.2.

### 2.1. The Passive Microwave Algorithm

The PMW algorithm developed by Markus et al. [5] uses a combination of three different parameters (Table 1) to detect characteristic changes in the daily Tb time series that develop during the melting season. Microwave emission of a scene containing sea ice and overlying snow cover is related to the melting condition of the snow and ice. Dry snow is characterized by volumetric scattering and has a low emissivity. When snow cover becomes wet, surface scattering dominates which increases the emissivity of the surface [28]. At the beginning of the melt season, freeze/thaw cycling as a result of transient weather systems or diurnal temperature fluctuation results in a rapid transition between periods of wet, melting snow (increasing emissivity) and periods of refreeze resulting in metamorphosis of the snow grains (lowering emissivity) [5,14,29]. Thus, the beginning of the MO period can be identified by a sharp jump in Tbs from the increase in liquid water content of snow and the onset of rapid temporal changes characteristic of the freeze/thaw cycling period [14,15].

To detect MO, the PMW algorithm uses vertically polarized Tbs at the 19 GHz (18 GHz from SMMR) and 37 GHz channels, hereafter noted as 19V and 37V (Table 1). The method distinguishes between two phases of melting—early MO and continuous MO. Early MO indicates the initial melting day, after which freeze/thaw cycles may occur, consistent with the “early melt” transition defined by Livingstone et al. [27]. The continuous MO date indicates the end of the freeze/thaw cycling period when melting occurs on a continuous basis through the summer until autumn freeze-up. The three criteria used to determine early and continuous MO include: the day-to-day change in spectral gradient ratio ( $\Delta GR_{ice}$ ) corrected for the influence of open water [5], the melt parameter P developed by Smith [14], and  $\Delta 37V$  which quantifies day-to-day variability in Tbs at the 37V GHz channel (Table 1). P and  $\Delta 37V$  are not corrected to account for SIC. However, Smith [14] found that small reductions in SIC have little effect on MO detection using P. Smith [14] has also shown that P fails to detect MO over areas containing mostly first-year ice. The PMW method utilizes multiple melting indicators, each with their own strengths and weaknesses to identify when the three melting criteria agree on a MO date [5]. To evaluate agreement of the melt criteria, a normalized weighting value is calculated based on thresholds representing the expected ranges of each criteria for sea ice [5]. The normalized weights are summed and the day of the year (DOY) with the largest weighted melting signal during the melt season is identified as the continuous MO date. The day of the year with the second largest weighted melting signal value is identified as the early MO date.

For each year, the PMW algorithm begins detecting MO on DOY 76 (17 March, 16 March during leap years) and operates on sea ice locations determined by an annual sea ice mask. The sea ice mask identifies grid pixels with at least 80% sea ice concentration (SIC) from the NASA Team Algorithm [30] for 5 days or more (consecutive or not) during the year (Table 1). Noisy results in time series analyses

of Tbs are expected [5]. To exclude false detection of melting dates from spurious Tbs a neighborhood test of the eight surrounding pixels is used to check for spatial continuity in the MO date determined for each grid pixel (Table 1). In some cases, an early MO date is not detected by the PMW method. This can be due to the immediate onset of continuous melting at a location, bypassing the early melt season freeze/thaw cycles [5]. In some cases a continuous MO date is not found when there is no clear melting signal from the weighted sum. Typically, the absence of a clear melting signal occurs in areas of young ice in the marginal ice zone [5] where relatively high background Tbs of the sea ice make it harder to distinguish the melting signal [14]. When no clear early or continuous MO signal is found, it is assumed that disintegration of the sea ice occurs very shortly after MO, thus, the day when the SIC (NASA Team) drops below 80% for the final time during the melt season is determined to be the MO date. The 80% concentration threshold is used for approximately 25% of pixels for a given year. Pixels in which the SIC threshold is used are generally located in marginal sea ice locations. The PMW algorithm is also used to determine the date of freeze-up; however, this work is focused only on MO for the years 1979–2012 for a consistent comparison of each dataset.

## 2.2. The Advanced Horizontal Range Algorithm

The AHRA developed by Drobot and Anderson [15] determines MO from daily, horizontally polarized Tbs at the 19 GHz (18 GHz from SMMR) and 37 GHz channels, hereafter noted as 19H and 37H. This method calculates a melt parameter from the Tbs known as the horizontal range (HR). HR is the difference between daily 19H and 37H Tbs (Table 1). The AHRA operates on the theoretical basis that the day-to-day variability in Tb increases as a result of freeze/thaw cycling during the early MO phase of the melt season [15]. As liquid water develops within the snowpack, surface scattering increases, resulting in increasing emissivity. However, scattering decreases with increasing wavelengths; thus, when snow becomes wet the emissivity increases more dramatically at higher frequencies (i.e., the 37 GHz channel) than at lower frequencies (i.e., 19 GHz) [31] resulting in the HR approaching 0 at MO [15]. The AHRA determines the date of earliest melting when liquid water first appears on the surface of snow grains [15], consistent with the Livingstone et al. [27] “early melt” season and similar to the PMW early MO date.

To detect melt, a threshold range from 4 K to  $-10$  K is applied to the HR. If the HR is greater than 4 K, wintertime conditions without melting are assumed to exist so the algorithm proceeds to the next day of the HR time series. The first DOY following the algorithm starting day, DOY 61 (2 March; 1 March during leap years), on which the HR value falls below the  $-10$  K threshold is flagged as the MO date. In cases when the HR falls within the threshold range, an analysis of the HR time series before and after the day in question is tested to identify if there is a change in the degree of temporal variability in the HR. This process, referred to as the 20-day window test, compares the range of HR values ( $HR_{\max} - HR_{\min}$ ) from the 10 days prior to and the nine days following the date being tested. If the difference in HR range after and before the date of interest are greater than 7.5 K ( $R_{\text{after}} - R_{\text{before}} > 7.5$  K), then MO is assumed. The 20-day window test serves a similar purpose as the  $\Delta 37V$  parameter used by the PMW method, which looks for an increase in the day-to-day variability observed in the Tb time series immediately following MO (Table 1) as a result of rapid freeze/thaw cycling and snow metamorphosis affecting the microwave signature. The 20-day window test provides a mechanism to filter out short-term effects on the Tbs from weather conditions. It is important to note that the HR parameter and Tbs are not corrected for the effect of day-to-day SIC changes. Therefore, the AHRA may recognize the development of open water (e.g., leads) and reductions in SIC as MO despite temperatures that are well below the freezing point [15]. AHRA MO dates are determined for sea ice areas where merged SIC from the NOAA/NSIDC Climate Data Record of Passive Microwave Sea ice Concentration Version 2 [32,33] are at least 50% on one or both of the first two days of March (Table 1).

### 2.3. Tbs and Calibration

To create long time series of MO dates using Tb data from multiple sensors over time, the daily gridded Tb data are calibrated using regression coefficients determined over specific sensor overlap areas to correct data to a baseline sensor commonly defined as the SSM/I from DMSP's F8 satellite [34–37]. For the PMW and AHRA, the Tbs are calibrated prior to determining MO dates by applying a series of algebraic corrections based on linear regression analysis to adjust the daily gridded Tb data (horizontally polarized for AHRA and vertically polarized data for PMW) from each sensor to the F8 baseline using chosen coefficients (i.e., to correct F17 to F13, then F13 to F11, then F11 to F8). SMMR data are corrected to the F8 baseline after Abdalati [35]. However, the inter-sensor calibration of the Tb record was performed inconsistently between the MO datasets for two reasons: (1) coefficients determined from different overlap regions were used for the PMW and AHRA corrections (i.e., the values used in the correction calculations were not the same); and (2) the correction calculations did not correct Tbs from the F13 to F11 values as intended affecting all MO dates from 1996–2012. Point 2 was identified and corrected in the most recent update (version 3) of the AHRA data used in this study [23] but still exists in the PMW dataset. Due to the inconsistencies in the Tb inter-sensor calibration corrections used by the PMW and AHRA algorithms, it is known that some uncertainties unrelated to the MO detection methodology are present in the long records of MO dates. Inter-sensor offsets in Tbs are generally small, <1.5 K [36] and are generally assumed to have a minor effect on MO dates given that the PMW and AHRA algorithms utilize day-to-day temporal changes in Tbs for MO detection [5,15]. However, slight offsets in Tbs between sensors do have the potential to affect the MO dates derived by these methods since the same threshold values are applied to the daily time series of Tbs in all years of the record. Slight offsets in the daily Tbs from sensor to sensor could potentially impact the day of MO detected by a MO algorithm, warranting the investigation reported in this work.

In addition to inter-sensor calibration differences, the datasets are produced using inconsistent versions of the SSM/I and SSMIS Tb source data. The PMW algorithm is produced using a combination of quality controlled Tbs from NSIDC's DMSP SSM/I-SSMIS Daily Polar Gridded Brightness Temperatures Version 4 dataset [38] and the near-real-time product [39] which is not subject to the same quality assessment and may contain unknown errors. The AHRA uses Tbs only from the prior quality-controlled Tb dataset at NSIDC. Therefore, some uncertainty in a comparison of MO dates from the AHRA and PMW datasets exists because the Tbs are not always from the same dataset. In the first part of our analysis, we use the published data as-is – with the inconsistent Tb inter-sensor calibration and other small differences as summarized in Table 1. In the second part of our analysis, we reproduce the AHRA and PMW MO dates using consistent source Tb data with identical inter-sensor calibration and sea ice masking in an attempt to remove as much error as possible so the MO data are more comparable.

### 2.4. Methodology for Original MO Date Comparison

The original MO datasets as distributed through NSIDC (for the AHRA) and NASA (for the PMW) are compared to report baseline statistics. Regions of the Arctic are defined as shown in Figure 1. References to the Arctic region in this work encompass all sea ice areas contained within the regions listed in Figure 1 excluding the pole hole north of 84.5°N where SMMR data were not collected. References to the Arctic Ocean in this work refer to eight regions: the Barents, Kara, Laptev, East Siberian, Chukchi, and Beaufort Seas, the central Arctic, and the Canadian Arctic Archipelago. Statistics reported for each MO dataset are calculated only over grid locations where a MO date exists for all years in the 1979–2012 record. Black stars labeled a, b, and c in Figure 1 indicate pixel locations in the Barents Sea, Laptev Sea, and central Arctic regions for case studies discussed in Section 3.1.

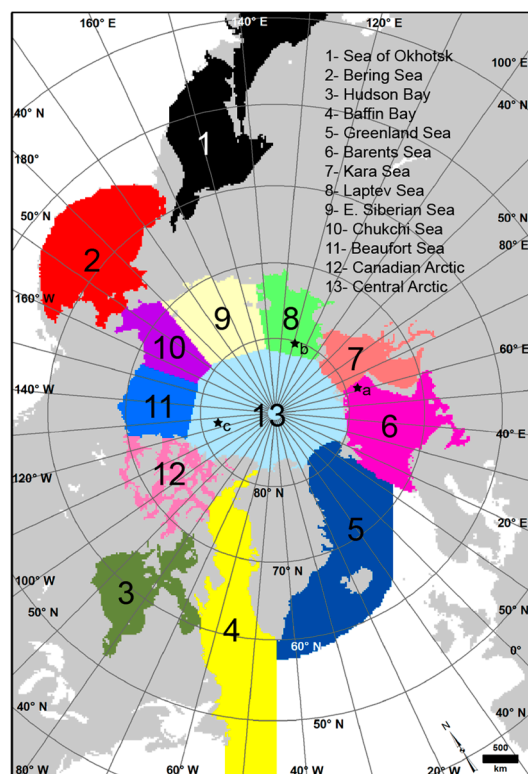


**Figure 1.** Regions of the Arctic. Stars indicate locations in the Barents Sea (a); Laptev Sea (b); and central Arctic (c) discussed in Section 3.1.

In many cases, the PMW method does not detect an early MO date as described previously (Section 2.1). Thus, the early MO dates from the PMW dataset are patchy, especially since 2007 (data collected by the F17 satellite). To make a comparison of early MO dates reported by the AHRA and PMW methods as comparable as possible a new PMW MO map for each year is created by combining the PMW early MO and continuous MO data. The PMW Combined MO date (hereafter PMWC) includes the early MO date where available and in cases where an early MO date is not found, the continuous MO date is substituted in place of the missing early MO date. Therefore, the PMWC annual maps consist of the earliest available MO date from the PMW. Following this point in the text, all references to PMW refer specifically to the algorithm methodology while PMWC refers to the combined MO dates/data.

Trends in the time series of regional mean MO dates are determined using a least squares linear regression and the significance of differences between AHRA and PMWC trends are determined using a two-tailed Student's *t*-test of the hypothesis that the slopes from the least squares linear regression are equal at the 95% confidence level. Local, pixel-wise trends for the AHRA and the PMWC are determined using a least squares linear regression with significance determined at the 95% confidence level.

MO dates from the AHRA and PMWC at three select locations (shown in Figure 1) are compared with mean daily 2 m surface air temperatures (SAT) from the International Arctic Buoy Program/Polar Exchange at the Sea Surface (IABP/POLES) [40].

### 2.5. Methodology for Adjusted MO Date Comparisons

For the second part of our analysis, the AHRA and PMW algorithms are applied to identical Tbs that have been corrected with calibration corrections from overlap areas as used in Anderson et al. [41] for their respective Tb polarizations (vertical for PMW and horizontal for AHRA). Other modifications are made to make the adjusted MO outputs as consistent as possible including: applying the AHRA

start-of-season sea ice masking method described in Section 2.2 to the PMW and a modification of the AHRA 20-day window technique for the years 1979–1987. The 20-day window in the original AHRA MO algorithm is applied over 20 days with Tb data without consideration for missing data days. To account for SMMR data that are only available every second day, we shorten the length of the 20-day window to apply over 20 calendar days, which is consistent with the rest of the daily Tb data record from SSM/I and SSMIS. The algorithm starting days, Tb channels, and melt criteria methodologies shown in Table 1 remain unchanged. The same land mask is used in both algorithms. Hereafter, the adjusted AHRA and PMWC data produced for this work are referred to as the AHRA-A and PMWC-A. The adjusted MO data are compared with the original data to determine how robust the algorithms are to calibration differences. Statistics reported for the adjusted MO data are calculated using the same methodologies used for the original MO data as described in Section 2.4. The comparison of the adjusted AHRA-A and PMWC-A data is intended to assess the differences between the algorithms with all else being equal to establish confidence in regional MO dates derived via passive microwave observations.

### 3. Results

#### 3.1. Examples of Algorithm Sensitivity

The AHRA and PMW methods rely on thresholds applied to melt criteria calculated from the daily time series of Tbs to detect changes in emissivity related to elevated wetness of the snow on sea ice caused by surface and internal melt processes. Examples from the Barents Sea (Figure 2), the Laptev Sea (Figure 3), and central Arctic (Figure 4), illustrate cases when the two MO methods produce very different MO dates in first-year ice locations (Figures 2 and 3) and one in which the methods agree closely on the date of MO in a multiyear ice location (Figure 4).

Figures 2–4 show the time series of melt parameters used by the PMW algorithm ( $\Delta GR_{ice}$ ,  $\Delta 37V$ , and P) at example single pixel locations (see Figure 1). During melt,  $\Delta GR_{ice}$  values are expected to approach 0 and return to more negative values as refreezing occurs (Figures 2a, 3a and 4a) [5]. Large peaks in  $\Delta 37V$  (Figures 2b, 3b and 4b) indicate increased day-to-day variability in Tbs present during melting. Thresholds applied to P at 460 K and 440 K (horizontal dotted lines) shown in Figures 2c, 3c and 4c are used to flag melting when the P value falls outside of the threshold range. P values above 460 K generally indicate melting in multiyear ice locations, and values of P below 440 K indicate melting for first-year ice regions [5]. The expected ranges of the three PMW melt parameters are normalized allowing the “strength” of each parameter’s melt signal to be summed (with equal weight) as shown in Figures 2f, 3f and 4f [5]. The weighted sum is shown (multiplied by 5) as the yellow curve. The day with the largest weight (Figures 2f, 3f and 4f) during the melt season is identified as the continuous MO date by the PMW algorithm; the secondary peak prior to the continuous MO date is identified as the early MO date.

The time series of HR used by the AHRA algorithm are shown in Figures 2d, 3d and 4d. The 4 K and  $-10$  K thresholds are shown as horizontal dotted lines. HR values above the 4 K threshold indicate dry snow conditions [15]. For each day, the algorithm checks if the HR value drops below the  $-10$  K threshold to assign the MO date. If the HR value falls below the 4 K threshold, but does not reach the  $-10$  K threshold, the 20-day window test is performed to assign the MO date by identifying the increased temporal variability in Tbs present during melt as described previously in Section 2.2. In each case shown in Figures 2d, 3d and 4d, the AHRA algorithm implements the 20-day window test when assigning the MO date. Figures 2g, 3g and 4g show the time series of daily POLES SAT for comparison with the MO dates derived by the AHRA and PMW algorithms.

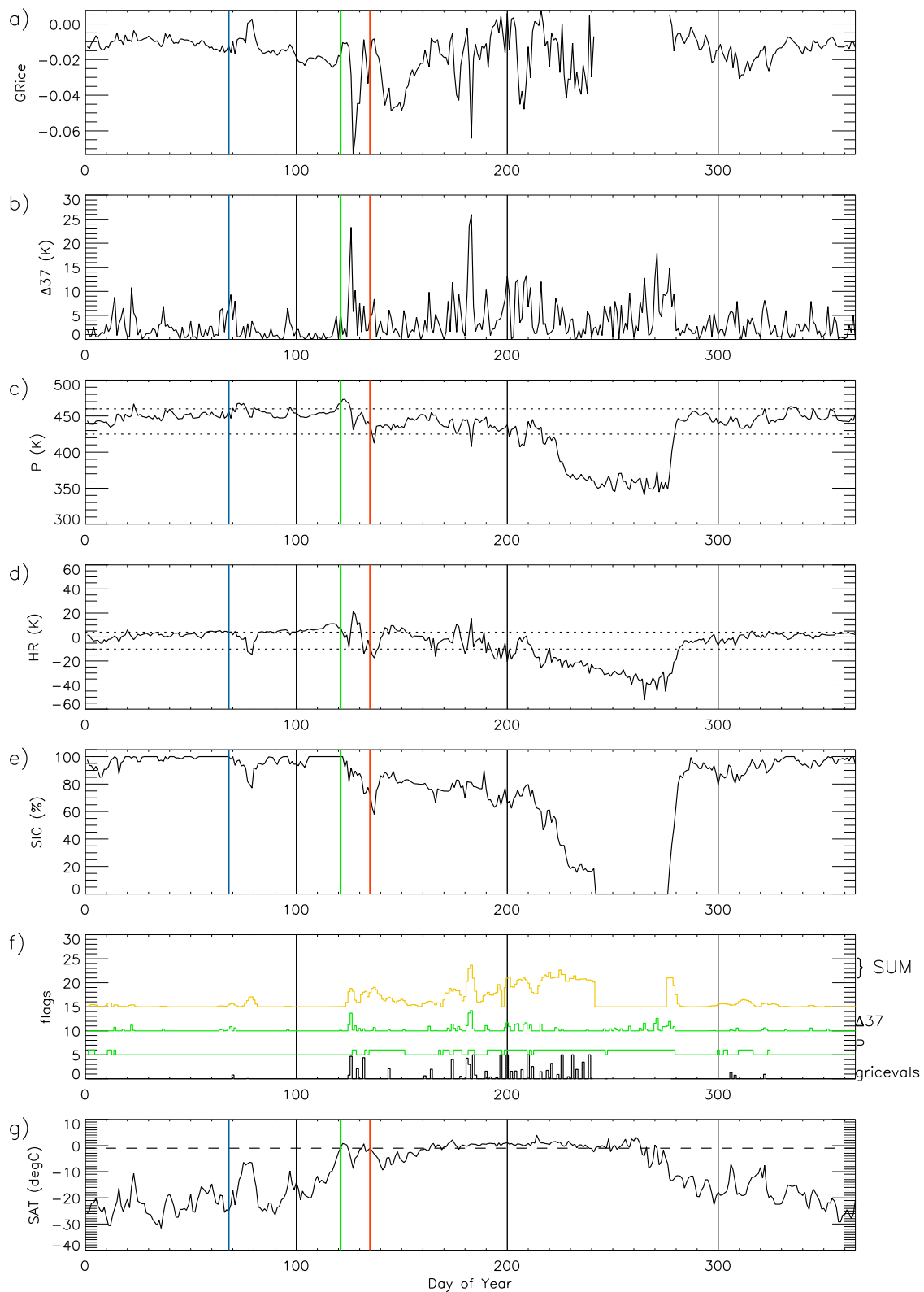


**Figure 2.** PMW MO parameters ((a)  $\Delta GR_{ice}$ , (b)  $\Delta 37V$ , and (c)  $P$ ), (d) AHRA HR, (e) NASA Team sea ice concentration, (f) PMW weighting flags (see text for details), and (g) POLES SAT from 1992 for case study location in the Barents Sea (78.3°N, 62.7°E). MO dates from AHRA (blue), PMWC (red), and first instance of SAT > 0 °C (green) are shown as vertical lines.

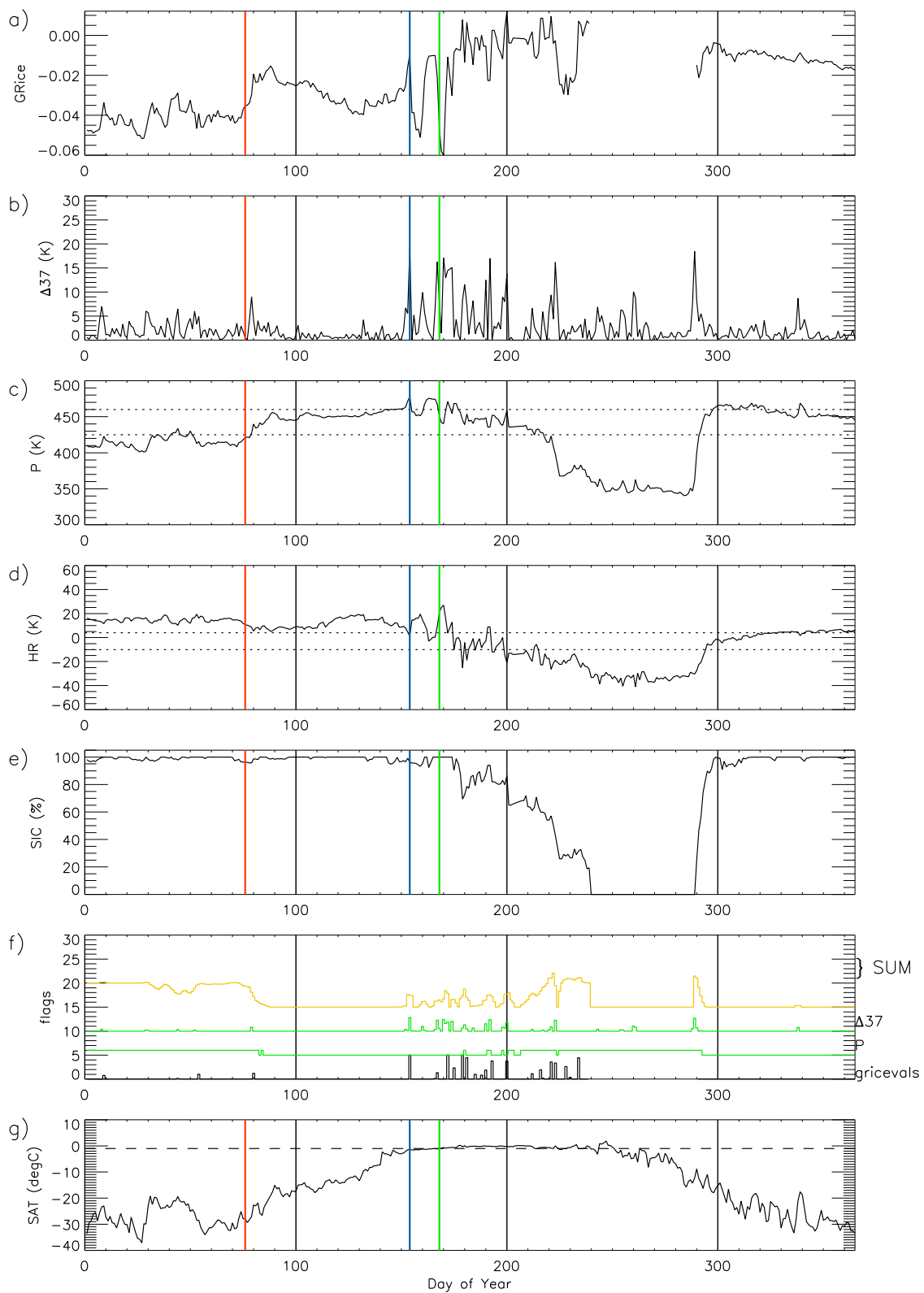


**Figure 3.** PMW MO parameters ((a)  $\Delta GR_{ice}$ , (b)  $\Delta 37V$ , and (c) P), (d) AHRA HR, (e) NASA Team sea ice concentration, (f) PMW weighting flags (see text for details), and (g) POLES SAT from 1995 for case study location in the Laptev Sea (79.7°N, 121.4°E). MO dates from AHRA (blue), PMWC (red), and first instance of SAT > 0 °C (green) are shown as vertical lines.

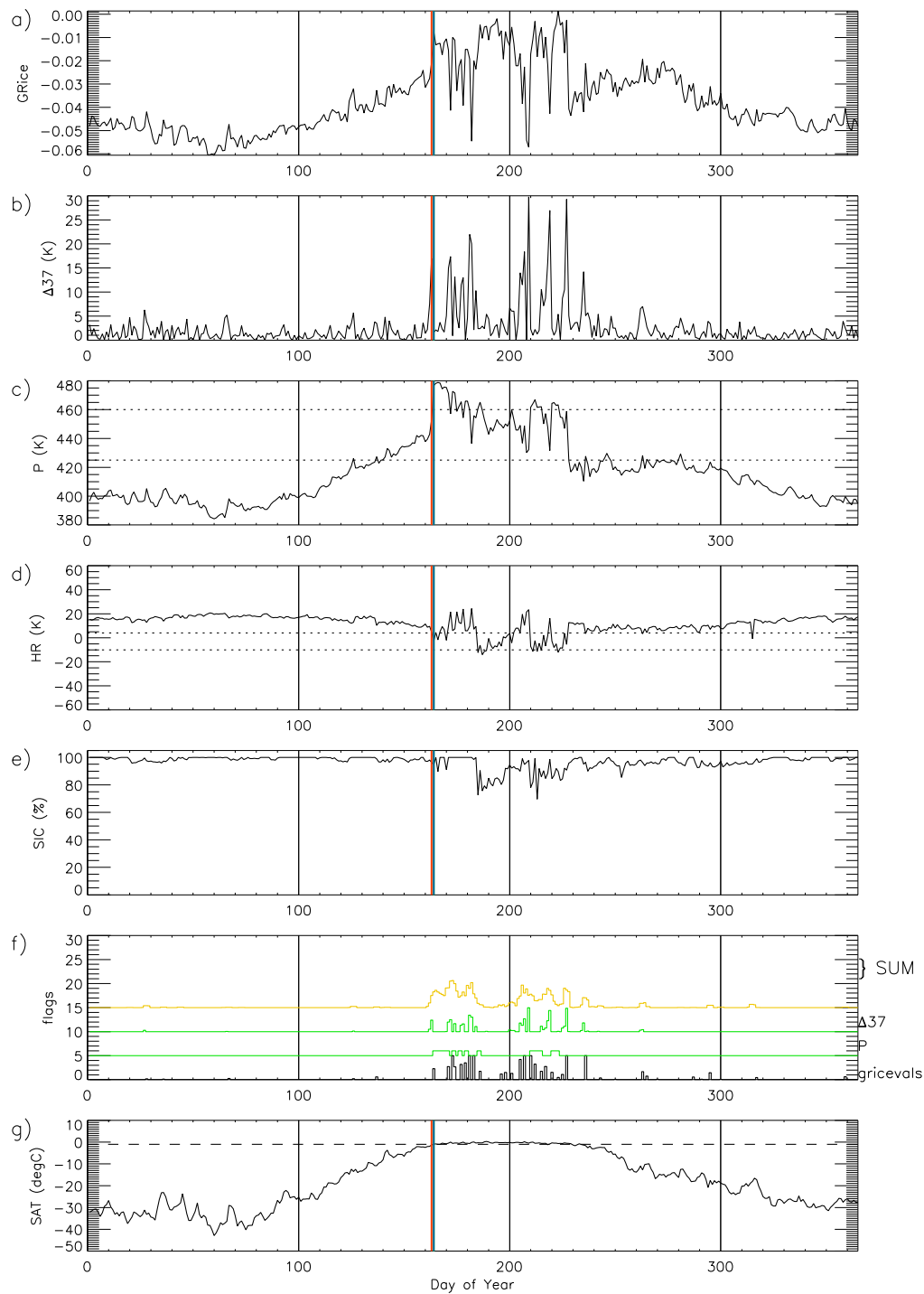


**Figure 4.** PMW MO parameters ((a)  $\Delta GR_{ice}$ , (b)  $\Delta 37V$ , and (c)  $P$ ), (d) AHRA HR, (e) NASA Team sea ice concentration, (f) PMW weighting flags (see text for details), and (g) POLES SAT from 1994 for case study location in the central Arctic ( $82.9^{\circ}N$ ,  $124.8^{\circ}W$ ). MO dates from AHRA (blue, obscured by SAT), PMWC (red), and first instance of SAT  $>0^{\circ}C$  (green) are shown as vertical lines.

### 3.1.1. The Barents Sea

In the Barents Sea (at  $78.3^{\circ}N$ ,  $62.7^{\circ}E$ ; location a in Figure 1) in 1992, the MO date from the AHRA is DOY 68 (7 March), while the PMWC MO date does not occur until DOY 135 (14 May), more than 2 months later (Figure 2). Since the discrepancy in the MO date is large, we describe the triggering factors identified by each algorithm used to define their respective MO date here.

On DOY 68 the SAT at the Barents Sea location is  $-25^{\circ}\text{C}$ , which is much too cold to suggest that melting is possible in the snow on sea ice (Figure 2g). So why does the AHRA identify DOY 68 as the MO date? In Figure 2d we see that the HR values generally fall within the 4 K to  $-10$  K threshold range throughout most of the year excluding a period during the summer between DOY 210–280. Recall from Section 2.2 that MO is detected when the HR drops below the  $-10$  K threshold or when the HR falls within the 4 K and  $-10$  K thresholds the 20-day window test is used to check for MO. In this case, the HR on DOY 68 falls just below the upper (4 K) threshold indicating that the 20-day window test was used to determine MO for this location (Figure 2d).

The HR for the 10 days prior to DOY 68 is 4 K with daily variation of only  $\pm 1$  K (Figure 2d). However, in the 9 days following DOY 68, the HR varies from 4 K on DOY 71 to  $-11$  K on DOY 77. Thus, the range of HR values ( $\text{HR}_{\text{max}} - \text{HR}_{\text{min}}$ ) for the 10 days before DOY 68 is 1 and the range of HR values for the 9 days after DOY 68 is 15. The difference between these two range values after and before DOY 68 ( $R_{\text{after}} - R_{\text{before}}$ ) is 14, which is greater than the 7.5 K window test threshold triggering MO in the AHRA algorithm.

In this case, the AHRA determined the MO date by identifying an increase in the day-to-day variability of the HR which is common during the early melting period; however, note that on DOY 77, the HR drops below the  $-10$  K threshold for the first time of the year (Figure 2d). The AHRA algorithm reports MO on DOY 68, 9 days before DOY 77 and on a day where the SAT is too cold for melt (Figure 2g). The 9-day difference is significant because it matches the length of the after period for the 20-day window test. In this case, the significant decrease in the HR did not occur until the very end of the 9-day window period, causing the algorithm to assign the MO date several days earlier than possible melting could have occurred. Without the 20-day window test, DOY 77 would have been flagged for MO based only on the HR falling below the lower ( $-10$  K) threshold.

The decrease in the HR seen on DOY 77 is coincident with a warming event that occurs over an 8 day period from DOY 72–79 (Figure 2g). During this event, SAT increases to  $-6^{\circ}\text{C}$ , a temperature that is still cold enough to suggest that little melting could occur (Figure 2g). Throughout this event SIC decreases by 25% (Figure 2e) in a pattern that is in step with the decreases in the HR (Figure 2d) suggesting that the AHRA is particularly sensitive to changes in SIC. Although the mean SAT during this event does not warm to  $0^{\circ}\text{C}$ , the warming pattern during DOY 72–79 (Figure 2g) is consistent with the passage of a low pressure system and associated warm front [12]. Atmospheric warming above the surface inversion associated with spring cyclones can initiate MO due to enhanced downwelling longwave radiation from thick cloud cover [8]. Further, precipitation and the evolution of the snow grain sizes under freezing surface conditions can impact the Tb signal [9]. The MO date on DOY 68 is unrealistic given the effect of the 20-day window test in this specific event; however given the uncertainties related to the SIC and atmospheric effects for this marginal, first-year ice location, it is also possible that no melting occurred on the later date (DOY 77) when the lower threshold condition was reached.

In this example from the Barents Sea, the PMWC MO date (DOY 135, 14 May) is much later than the AHRA MO date DOY 68 (Figure 2). Recall that MO in the PMW algorithm is determined by the sum of three equally weighted normalized values calculated from the values  $\Delta\text{GR}_{\text{ice}}$ ,  $\Delta 37\text{V}$ , and P. The PMWC MO date detected on DOY 135 is primarily the result of a drop in the P parameter beginning on DOY 122, which results in P crossing the lower (440 K) threshold for the first time of the year (Figure 2c). This pixel location is a first-year ice location, thus the PMW algorithm recognizes a melting signal when P falls below the lower threshold. Peaks in  $\Delta 37\text{V}$  (Figure 2b) and  $\Delta\text{GR}_{\text{ice}}$  values approaching 0 (Figure 2a) indicating potential melt are apparent for several other days prior to the MO date DOY 135; however, because P does not reach the lower threshold on those other days, the sum of the weights (Figure 2f) are not large enough for the algorithm to assign MO. Since P is the only melt parameter that is given a discreet threshold to indicate melt, P seems to be the controlling factor in the PMW algorithm's choice for the MO date. In this case, the largest peak in the sum of weights near DOY 183 is assigned as the continuous MO date, and the second largest peak, on DOY 135, becomes

the PMWC date shown in Figure 2. SAT reaches 0 °C (green vertical line in Figure 2) for the first time on DOY 121 (20 April) (Figure 2g). Following this date, SIC begins to drop to 55% (Figure 2e), the  $\Delta GR_{ice}$  value remains relatively high, and a large magnitude peak in  $\Delta 37V$  occurs on DOY 126 nearly coincident with a drop in P on DOY 127 suggesting that the MO parameters are detecting some melt signal following the warming of SAT above 0 °C. The peaks in P above the upper (460 K) threshold (Figure 2c) coincide with local peaks in SAT near DOY 73, 97, and 121 on which SAT reach the melting point (Figure 2g). However, it is not until DOY 135 that the P value crosses the lower threshold for first-year ice preventing the algorithm from assigning MO on an earlier date.

### 3.1.2. Laptev Sea

In contrast to the Barents Sea case described above, a case in which the PMWC MO date is extremely early when compared to the AHRA occurs in the Laptev Sea (at 79.7°N, 121.4°E, location b in Figure 1) in 1995 (Figure 3). The AHRA MO date at this location is DOY 154 (3 June), approximately two weeks before the daily mean SAT warms to 0° C on DOY 168 (17 June) (Figure 3g). The 20-day window test is used to determine this MO date since the HR falls within the 4 K to −10 K range for the first time on DOY 154 (Figure 3d). The AHRA identifies the increase in day-to-day variability of the HR time series before and after DOY 154 and assigns the MO date. The AHRA MO date appears to be reasonable in this case given that the daily mean SAT is very near 0° C at this time (Figure 3g), thus it is likely that some thawing is occurring even for short periods of the day which would be evident in the passive microwave Tbs as rapid temporal changes from metamorphosis of snow grains during freeze/thaw cycling.

The PMWC MO date on DOY 76 (17 March) is followed by an increase in  $\Delta GR_{ice}$  (Figure 3a) and a peak in  $\Delta 37V$  (Figure 3b) a few days after. In this case, values for P are below the lower (440 K) threshold throughout the beginning of the year (Figure 3c). DOY 76 is the earliest possible MO date determined by the PMW method (Table 1) and on DOY 76, the SAT is around −25 °C, too cold for MO (Figure 3g). The PMWC MO date occurs too early in this case, largely due to the P value being outside of the expected threshold values early in the year. This is similar to the Barents Sea case described above in which the AHRA MO date is unrealistically early when the SAT is too cold to suggest melting. The P value developed by Smith [14] was first applied over perennial sea ice only. Over first-year ice, Smith's [14] algorithm commonly failed to detect MO with skill. Thus, the P parameter may not be able to reliably detect MO in this location with the currently used algorithm thresholds since it primarily consists of first-year ice. Interestingly on DOY 154, the AHRA MO date, coincident peaks in  $\Delta GR_{ice}$  (Figure 3a) and  $\Delta 37V$  (Figure 3b) indicate a melting signal that is larger than for the PMWC MO date on DOY 76. There is even a modest peak in the P value above the upper (460 K) threshold, which would suggest melt if this location was multiyear ice (Figure 3c). However, the size of the peak in the sum of weights is not as large as the high sum values at DOY 76 (Figure 3f), thus the PMW algorithm does not assign MO on DOY 154 which appears to be a more realistic MO date. On examining the weighted sum values (yellow curve in Figure 3f), high sum values are present throughout much of the first 80 days of the year including values for DOY 68–74 that are slightly larger than the sum value on the MO date DOY 76. However, because the PMW algorithm does not begin MO detection prior to DOY 76 (Table 1), one of these earlier days cannot be flagged for MO. That is, the MO date on DOY 76 is somewhat arbitrarily based on the algorithm starting date (DOY 76) even though the (unrealistic) MO date could have been detected earlier.

### 3.1.3. Central Arctic

The third case is an example of when the AHRA and PMWC agree very closely on the date of MO (Figure 4). During the 1994 melt season in the central Arctic region (at 82.9°N, 124.8°W, location c in Figure 1), the PMWC MO date is DOY 163 while the AHRA MO date is DOY 164 (12–13 June). The three melt parameters used by the PMW method clearly identify the day of MO (Figure 4a–c) while the AHRA identifies the increase in variability of the HR time series immediately after the HR drops just

below the 4 K threshold, initiating the 20-day window test to identify the MO date (Figure 4d). In this case, the MO dates from the PMW and AHRA occur at the same time that SAT warms to 0 °C on DOY 164 (the vertical line indicating MO timing according to the SAT is fully obscured by the AHRA MO date shown with the blue line) (Figure 4g), suggesting that algorithms identified a realistic MO date.

### 3.1.4. Case Studies Summary

The previous examples show two cases in which the algorithms assign very different MO dates and one case in which the two methods agree closely on a reasonable MO date in different locations of the Arctic. The examples presented here are not an exhaustive analysis of all possible situations where the algorithms may produce inconsistent MO dates, but they illustrate a few non-unique situations that occur when the AHRA and PMW MO data are compared. Based on analysis of these and other examples, the algorithms tend to perform less consistently in first-year ice and marginal ice regions where uncertainty in the Tb data is larger due to weather effects including cloud liquid water and increased water vapor [42] and higher background Tbs of first-year sea ice which can make the melting signal harder to identify [14]. In some cases, especially in the southern-most ice extent regions, where melting would occur earlier in the year, the arbitrary start date of the algorithms (Table 1) controls the date of MO when the algorithm parameter time series (as shown in Figure 3) begins the year showing “melt-like” signatures. It is known that over much of the sea ice in the peripheral seas, the AHRA has a MO date of DOY 61 (1 March), the first day of the melt season defined in the AHRA [23] (described further in Section 3.2). This indicates that the HR prior to the start of the melt season is already below the threshold values set by the method; thus, MO occurs immediately. The same issue can occur in the PMW method as shown in Figure 3, however, it appears less frequently in the PMWC MO dates than it does in the AHRA MO dates. In this case, the MO date is assigned DOY 76 even though the cold SAT suggests melting is impossible (Figure 3g). The arbitrary melt season start dates in the AHRA and PMW algorithms could influence regional means and statistical summaries primarily in the peripheral seas where sea ice is relatively thin and young. In future algorithm updates, it would be beneficial to reconsider the algorithm start dates used by the AHRA and PMW and further, to consider adjustment of the threshold values used in southerly latitude bands to avoid extremely early MO signals as appear in the AHRA MO dates.

The Barents Sea case shown in Figure 2 is interesting as well because it illustrates a case where the sensitivity of the thresholds for both algorithms produce very different MO dates. The AHRA is sensitive to a small event that occurs earlier in the year causing the HR to fall just below the lower threshold for a short period of time (Figure 2d). The PMW method (which was not calculated for this event as it occurred prior to the DOY 76 start date) and its algorithm parameters are relatively insensitive to the magnitude of Tb changes that occurred at this time and the lower threshold for the P parameter was not reached (Figure 2c). The PMWC MO date does not occur until two weeks after the SAT reaches the melting point. Another important point represented with this case is that the AHRA is 9 days early in the detection of the MO date due to the 20-day window testing method used by the algorithm. The early offset is likely present in many other locations, especially in the southernmost ice locations, where the HR falls within the AHRA thresholds. However, this specific offset is not always present in the AHRA as in the central Arctic example described above (Figure 4d). In general, better agreement between MO methods are expected in areas of the central Arctic where sea ice is typically multiyear ice and mean MO dates are climatologically unaffected by algorithm start date artifacts.

### 3.2. Comparison of Original and Adjusted MO Dates

From the original MO data, the earliest melting regions in the Arctic are generally the southern-most regions along the periphery of the sea ice cover [5,23]. This is expected given that the regions are located at lower latitudes where SAT is seasonally warmer than locations nearer the North Pole. This pattern is shown in the mean PMWC and AHRA MO dates over the 1979–2012 climatology in Figure 5a,b. Note that the scales are the same in Figure 5a,b,d,e. The earliest melting regions

include: the Sea of Okhotsk, Bering, Barents and Greenland Seas, and the southern portion of Baffin Bay (warm colors in Figure 5a,b). The general pattern of melting area spreading northward throughout the spring and summer is present for both the AHRA and PMWC (Figure 5a,b); however, there are some noticeable inconsistencies in the mean differences expressed as PMWC–AHRA (Figure 5c). First, the AHRA reports an earlier MO date than the PMWC in nearly all locations. The only negative differences in which the PMWC dates are earlier than the AHRA (Figure 5c, in blue) are primarily located in the northern Canadian Arctic Archipelago region and in the adjacent part of the central Arctic region. Also, large differences occur along the coastlines (Figure 5c,d, in red and magenta) and are very obvious in the Okhotsk region, in the Bering and Chukchi Seas, and along the southern coast of Greenland. The unusual MO date pattern along these coastlines is most likely an artifact of noise from land–ocean spillover effects [42] present in the Tbs.

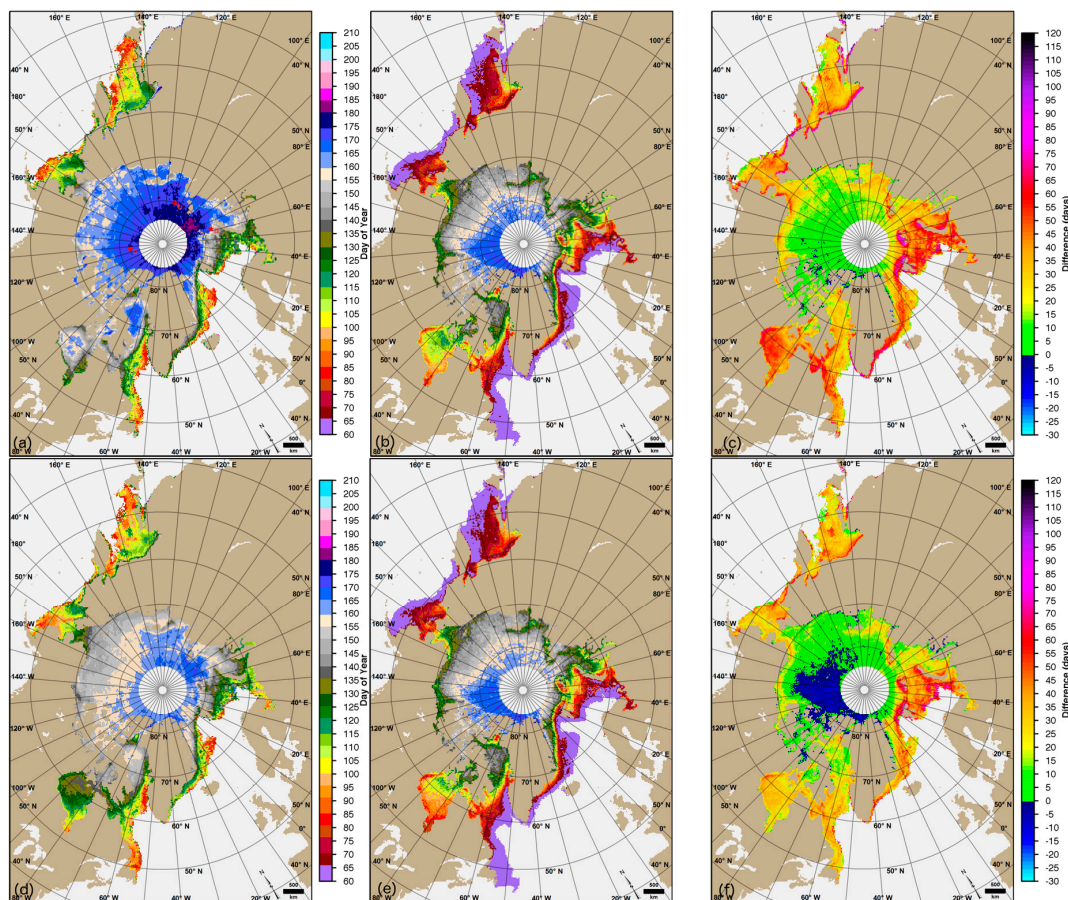


**Figure 5.** Mean MO dates (1979–2012) for the (a) PMWC; (b) AHRA; (d) PMWC-A; (e) AHRA-A; and differences expressed as (c) PMWC–AHRA and (f) PMWC-A–AHRA-A. Pixels in white indicate areas of no data. Locations a, b, and c noted in Figure 1 are shown in (a) for reference.

For the Arctic region, the mean MO date as reported by the AHRA occurs on DOY 122, May 2nd (Table 2), while the mean MO date as reported by the PMWC occurs 20 days later on DOY 142, May 22nd. Regionally, the mean differences are as low as 1.1 days in the central Arctic (Table 2). The largest mean differences are greater than 30 days and occur in the peripheral sea ice regions including the Barents, Greenland, Okhotsk, and Bering Seas, and in Baffin and Hudson Bays (Table 2) where sea ice is typically first-year ice [43]. In some cases, the apparent early offset in the AHRA mean MO date is related to the algorithm detecting MO earlier than the day on which the HR indicates melting due to the 20-day window technique as described in Section 3.1.4. However, the AHRA MO dates do not appear to be systematically nine days earlier than the PMWC mean MO dates (Table 2).

If the AHRA MO dates were consistently nine days early a simple adjustment could be applied to the MO dates; however, the regional mean differences (which range from 1.1 to 38.3 days difference as shown in Table 2) indicate that the differences in observed MO dates from the AHRA and PMWC are more complex.

**Table 2.** Melt onset date regional <sup>a</sup> means, standard deviations, and the difference between means (days) and trends <sup>b</sup> (days-decade<sup>-1</sup>) for 1979–2012.

Region	AHRA v3			PMW Combined			Mean Diff. (PMW–AHRA)
	Mean	St. Dev.	Trend	Mean	St. Dev.	Trend	
Arctic-All	121.9	5.2	−4.5 *	142.1	3.6	−1.6	20.2
Sea of Okhotsk	74.1	3.9	−1.0	110.0	6.3	2.4	35.9
Bering Sea	72.7	4.6	1.7	106.4	6.9	−0.4	33.7
Hudson Bay	106.6	8.6	−2.8	126.8	8.7	−4.5	20.2
Baffin Bay	101.8	5.7	−0.3	131.9	7.2	−1.5	30.1
Greenland Sea	98.0	7.6	0.8	133.5	8.6	−3.4	35.5
Barents Sea	84.3	10.4	−7.5 *	122.6	12.6	−6.7	38.3
Kara Sea	128.9	12.9	−9.3 *	148.4	10.1	−5.9 *	19.5
Laptev Sea	145.0	11.7	−8.2 *	156.7	8.0	−3.0	11.7
East Siberian Sea	150.1	14.5	−11.8 *	153.4	5.6	−1.4	3.3
Chukchi Sea	136.3	12.7	−8.3 *	144.8	8.2	−2.1	8.5
Beaufort Sea	148.2	9.9	−7.2 *	151.8	7.5	−2.5	3.6
Canadian Archipelago	149.2	7.7	−4.6 *	152.9	6.0	−2.0	3.7
Central Arctic	159.6	9.3	−8.1 *	160.7	5.2	−2.7	1.1

<sup>a</sup> Regions are defined as in Figure 1; <sup>b</sup> Bold values indicate statistical significance at the 95% confidence level or above. An \* indicates statistical significance at the 99% confidence level.

Statistically, the latest observed MO from both the PMWC and AHRA occurs in the central Arctic region (Table 2); however, the methods disagree in the specific location of latest MO. The AHRA consistently identifies the mean latest melting locations in the western half of the central Arctic, north of Greenland and the Canadian Arctic Archipelago (Figure 5b) in regions that generally have the largest multiyear ice fraction. This result is consistent with the findings of Smith [14] who found latest MO dates determined using the P parameter (a component of the PMW algorithm) over perennial sea ice are centered near Greenland and the Canadian Arctic Archipelago. Figure 5c indicates that the PMWC MO dates in this area are slightly later than the AHRA (0 to +10 days difference, green) for most of the area and in a few locations the PMWC MO date is earlier than the AHRA (−10 to 0 days difference, dark blue). By contrast, the latest mean PMWC MO dates occur in the eastern half of the central Arctic region, immediately north of the Kara and Barents Seas (Figure 5a). The PMWC MO dates in this area (in purple Figure 5a) are later than any observed MO dates in the AHRA mean MO dates, ranging from approximately 20–30 days difference (Figure 5c). The discrepancy in location of latest observed MO suggests that AHRA method may be more sensitive to the fraction of older, multiyear ice than the PMW method.

Inter-annual variability in MO dates is generally higher for Arctic Ocean regions in the eastern hemisphere, especially in the Kara and Barents Seas where the standard deviation of the MO dates are 12.9 (AHRA) and 10.1 (PMWC) days and 10.4 (AHRA) and 12.6 (PMWC) days respectively (Table 2). Standard deviations in AHRA mean MO date are larger than for the PMWC in all regions within the Arctic Ocean except the Barents Sea (Table 2). The region with the greatest standard deviation from the AHRA is the East Siberian Sea (14.5 days). The PMWC standard deviation for the East Siberian Sea is much smaller (5.6 days) (Table 2). Less overall variability in the MO dates from the PMW is expected given that the method utilizes several melt criteria in addition to the spatial neighborhood test in contrast to the AHRA which uses only one melt criteria. Higher variability in MO dates is attributed to variability in spring weather systems that initiate MO; however, differences in the MO algorithm methodology likely contribute to some of the variation in the means and standard deviation reported in Table 2.

Local trends in original MO dates for 1979–2012 are shown in Figure 6. Statistically significant negative trends at the 95% confidence level from the AHRA indicating earlier MO exist over nearly all of the Arctic Ocean with the largest negative trends occurring in the northern Barents Sea (Figure 6b). Small areas of significant positive trends, which indicate MO occurring later in the year, exist in the Bering Sea and near the coastlines in the Sea of Okhotsk, the Canadian Arctic Archipelago and in northern Hudson Bay (Figure 6b). The PMWC negative local trends are not as dominantly significant in the Arctic Ocean as for the AHRA trends (Figure 6a); however, the larger negative trends from the PMWC occur in the northern Barents Sea, consistent with the AHRA. The positive local trends that exist in the AHRA are largely absent from the PMWC and, notably, these locations are dominantly negative in the PMWC, especially in northern Hudson Bay (Figure 6).

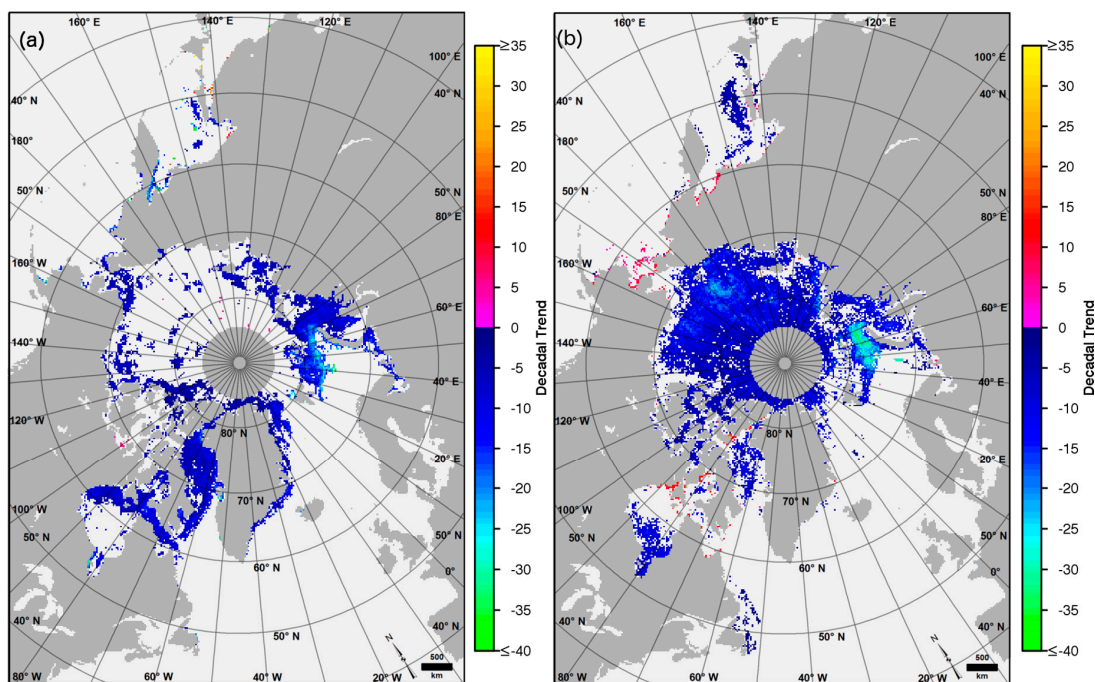


**Figure 6.** Statistically significant decadal trends ( $\text{days}\cdot\text{decade}^{-1}$ ) for (a) PMWC; and (b) AHRA MO dates over 1979–2012. Trends are significant at the 95% level. Areas with no data and insignificant trends are shown in white.

The adjusted mean MO dates for the AHRA-A and PMWC-A from our modified processing are shown in Figure 5d,e. The mean AHRA-A MO dates (Figure 5e) compare closely to the AHRA mean MO dates (Figure 5b). The PMWC-A mean MO dates (Figure 5d) are noticeably earlier than the PMWC (Figure 5a) for most of the Arctic Ocean and in Hudson Bay. The latest melting region in the PMWC north of the Kara Sea (Figure 5a, in purple) is still the latest melting area in the PMWC-A (Figure 5d); however, MO dates are approximately 15 days earlier in the PMWC-A than they are in the PMWC. The differences (expressed as PMWC-A–AHRA-A) shown in Figure 5f indicate smaller differences between the PMWC-A/AHRA-A MO dates than observed in the original PMWC/AHRA differences for most of the Arctic (Figure 5c). Regions with smaller differences (Figure 5f, greens) occur in the coastal regions of the Arctic Ocean including parts of the Kara, Laptev, East Siberian, Chukchi, Canadian Archipelago, Baffin Bay, and Hudson Bay regions. A larger proportion of negative PMWC-A/AHRA-A differences occur in the central Arctic extending into the northern Beaufort Sea and Canadian Arctic Archipelago regions. These negative differences (Figure 5f, in blue) show a larger area of the Arctic in which the PMWC-A MO dates occur earlier than the AHRA MO dates.

Recall from Section 2.5 that the modifications to the AHRA used to create the AHRA-A data are relatively minor; thus, only small changes are expected in the mean MO dates for the AHRA/AHRA-A

comparison. By contrast, a more significant change applied to PMWC-A data is the change to the inter-sensor calibration of the brightness temperatures for most of the study period. The results shown in Figure 5a,d suggest that the corrections applied to the PMWC-A which generally have only a small effect on passive microwave Tbs [36] can have a much more noticeable effect in threshold based products such as the MO dates derived from corrected Tbs.

### 3.3. Trend and Average Offset Comparisons

To identify changes in long-term MO date observations due solely to consistent source data, inter-sensor calibration inconsistencies, and masking methodology, we compare average offsets of the mean MO date time series and trends from the time series of annual mean MO date for the original AHRA and PMWC MO dates and for our adjusted MO dates. Here, average offsets expressed as PMWC–AHRA and PMWC-A–AHRA-A (reported in Table 3) are calculated from the regional mean MO date as shown in Table 2. The offsets represent the mean difference between the AHRA/PMWC curves shown in Figure 7 and the AHRA-A/PMWC-A curves shown in Figure 8. As described in Section 2.4, trends for the original and adjusted MO date are determined from a least squares linear regression applied to the time series of mean MO date for the Arctic and sub-regions (Figure 1). A simple Student's *t*-test of the hypothesis that the slopes from the regression are equal at the 95% confidence level is used to test similarity of the slopes. Cases when we fail to reject the hypothesis are indicated in Table 3 with a Y (for yes) indicating that the slopes are equal/similar. Cases when we reject the hypothesis are indicated in Table 3 with an N (for no) indicating that the slopes are not equal/similar. The highest confidence in MO date from both algorithms occurs when the overall trend in the time series of mean MO date is statistically similar based on the slope test and where the average offsets from the mean MO date time series is minimized (near zero). The results of the slopes tests are presented in Table 3 for the original (AHRA and PMWC) MO dates and the adjusted (AHRA-A and PMWC-A) MO dates. Slopes that are statistically similar indicate that both datasets are capturing the same trend in mean MO over the 34-year record, although offsets in the overall mean MO date for the Arctic and sub-regions may still exist.

**Table 3.** Trends <sup>a</sup> (days-decade<sup>-1</sup>), average offsets <sup>b</sup> (days), and slope comparison <sup>c</sup> results for the AHRA v. PMWC and AHRA-A v. PMWC-A

Region	AHRA v. PMWC Comparison				AHRA-A v. PMWC-A Comparison			
	AHRA Trend	PMWC Trend	Avg. Offset	Slopes Equal? (Y/N)	AHRA-A Trend	PMWC-A Trend	Avg. Offset	Slopes Equal? (Y/N)
Arctic-All	<b>-4.5 *</b>	<b>-1.6</b>	20.2	N	<b>-2.2 *</b>	<b>-3.7 *</b>	24.1	N
Sea of Okhotsk	-1.0	<b>2.4</b>	35.9	N	<b>1.4</b>	0.8	38.6	<b>Y</b>
Bering Sea	<b>1.7</b>	-0.4	33.7	<b>Y</b>	<b>2.6</b>	-2.1	35.9	<b>Y</b>
Hudson Bay	-2.8	<b>-4.5</b>	20.2	<b>Y</b>	<b>4.0</b>	<b>-4.0</b>	27.4	N
Baffin Bay	-0.3	-1.5	30.1	<b>Y</b>	0.9	<b>-3.3</b>	33.6	<b>Y</b>
Greenland Sea	0.8	<b>-3.4</b>	35.5	N	2.3	<b>-6.2 *</b>	39.4	N
Barents Sea	<b>-7.5 *</b>	<b>-6.7</b>	38.3	<b>Y</b>	<b>-6.0 *</b>	<b>-9.7 *</b>	42.4	<b>Y</b>
Kara Sea	<b>-9.3 *</b>	<b>-5.9*</b>	19.5	<b>Y</b>	<b>-8.6 *</b>	<b>-6.0 *</b>	21.4	<b>Y</b>
Laptev Sea	<b>-8.2 *</b>	<b>-3.0</b>	11.7	N	<b>-7.2 *</b>	<b>-3.9</b>	14.2	<b>Y</b>
East Siberian Sea	<b>-11.8 *</b>	-1.4	3.3	N	<b>-9.6 *</b>	<b>-2.7</b>	5.8	N
Chukchi Sea	<b>-8.3 *</b>	-2.1	8.5	N	<b>-6.7 *</b>	<b>-2.8</b>	10.4	<b>Y</b>
Beaufort Sea	<b>-7.2 *</b>	-2.5	3.6	N	<b>-6.3 *</b>	<b>-4.2 *</b>	4.8	<b>Y</b>
Canadian Archipelago	<b>-4.6 *</b>	-2.0	3.7	<b>Y</b>	<b>-2.8</b>	<b>-2.4</b>	6.5	<b>Y</b>
Central Arctic	<b>-8.1 *</b>	<b>-2.7</b>	1.1	N	<b>-5.2 *</b>	<b>-4.5 *</b>	4.9	<b>Y</b>

<sup>a</sup> Bold trends indicate statistical significance at the 95% confidence level or above. An \* indicates statistical significance at the 99% confidence level; <sup>b</sup> Expressed as PMWC–AHRA and PMWC-A–AHRA-A; <sup>c</sup> The slope comparison indicates regions where the slopes of the time series are equal (Y) or unequal (N) based on a Student's *t*-test for slope differences at the 95% confidence level.

### 3.3.1. Original AHRA and PMWC Trend Comparison

The time series of regional mean MO date for the AHRA and PMWC MO dates are remarkably different (Figure 7, Table 3). The relatively early MO dates that exist in the AHRA data when compared to PMWC MO dates (e.g., Table 2, Figure 5) are apparent as larger offsets between the curves in Figure 7, however, it is important to note that a systematically early offset is not observed across all regions. The average offsets for each region are generally larger outside of the Arctic Ocean, including differences greater than 30 days for the Sea of Okhotsk, Baffin Bay, Bering, Greenland, and Barents Seas (Table 3). In most cases, the minima (earlier MO) and maxima (later MO) of the time series are in-phase, although the relative magnitude of the peaks can differ (Figure 7). It is important to note that stepwise jumps at sensor changes (indicated on Figure 7 by vertical dotted lines) are largely absent.

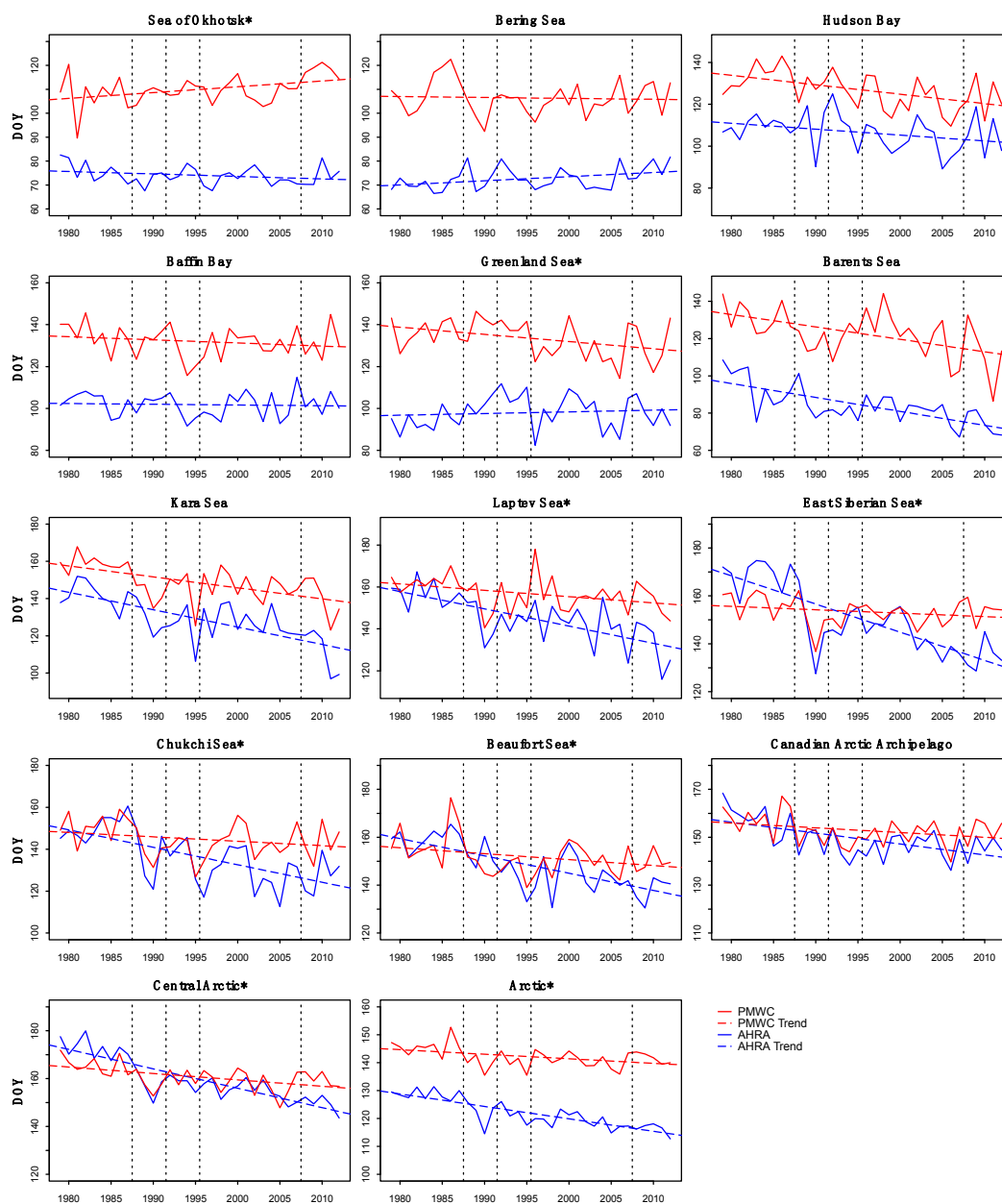


**Figure 7.** Annual mean MO date (DOY) for the AHRA and PMWC methods for 1979–2012. Least squares linear regression trends are shown as dashed lines. Vertical dotted lines indicate when changes in passive microwave satellite sensors occur. Trends are significantly different at the 95% confidence level based on a Student's *t*-test in regions indicated with an asterisk.

Regional trends in annual mean MO date from a least squares linear regression for the AHRA and PMWC are shown in Figure 7. The largest trend difference is observed in the East Siberian Sea where the AHRA trend is  $-11.8$  days·decade<sup>-1</sup> (statistically significant at the 99% confidence level) and the PMWC reports a trend of  $-1.4$  days·decade<sup>-1</sup> (not statistically significant) (Table 3). In the central Arctic where mean MO dates from the AHRA and PMWC are very similar (Table 2), the trends are very different at  $-8.1$  days·decade<sup>-1</sup> (statistically significant at the 99% confidence level) for the AHRA and  $-2.7$  days·decade<sup>-1</sup> (statistically significant at the 95% confidence level) for the PMWC (Table 3). The sign of trends is consistent for both the AHRA and PMWC in nearly all regions except in the Greenland, Bering, and Okhotsk regions where the sign of trends for the two MO methods diverge (Figure 7, Table 3).

Based on tests of the slope, the trends of the annual mean MO dates for the AHRA and PMWC (Figure 7) are significantly different at the 95% confidence level for the whole Arctic and regionally in the Sea of Okhotsk, Greenland, Laptev, East Siberian, Chukchi, and Beaufort Seas and in the Central Arctic (Table 3). The slopes for the AHRA and PMWC are equal in the Bering, Hudson, Baffin, Barents, Kara, and Canadian Archipelago regions (Table 3). Despite the slopes being equivalent for these regions, the average offsets (Table 3) between the two methods are large in the Bering (33.7 days), Barents (38.3 days), and Kara Seas (19.5 days), and in Hudson (20.2 days) and Baffin Bays (30.1 days).

The results presented in Figure 7 indicate several inconsistencies between the AHRA and PMWC MO data including (1) an early, regionally variable offset of the AHRA MO dates; (2) disagreement in the magnitude of the slope for nearly all regions and in some cases the sign of trends; and (3) comparatively larger offsets in the marginal sea ice areas. The AHRA and PMWC MO dates are dissimilar for much of the Arctic sea ice indicating that there are significant differences in the sensitivities of each algorithm to the sea ice conditions which vary regionally and that the MO date products cannot be used interchangeably by data users.

### 3.3.2. Adjusted AHRA-A and PMWC-A Trend Comparison

Trend comparisons from the AHRA-A and PMW-A are shown in Figure 8. For easier comparison with the AHRA and PMWC time series, the AHRA and PMWC curves (as shown in Figure 7) are included in Figure 8 (thin, solid curves) for reference. The results of the slopes test for the AHRA-A and PMWC-A MO dates (Table 3) indicate that the slopes are significantly different at the 95% confidence level in the East Siberian, Greenland, and Hudson Bay regions and for the whole Arctic. The results of the slopes tests on the adjusted MO data show improvement in the consistency of the trends in mean MO date for the Beaufort, Chukchi, Laptev, Okhotsk, and central Arctic regions over the original data where the trends are now statistically similar (Table 3). Interestingly, the offsets increase slightly for all regions (Table 3), ranging from 1.2 days in the Beaufort Sea to 7.2 days in Hudson Bay with an average increase of 3.2 days for all regions (Table 3).

The changes to the time series of MO date when the adjusted data are compared to the original data are generally small (Figure 8). Larger differences occur during the SMMR years (1979–1987) especially apparent in Hudson Bay, Sea of Okhotsk, Bering Sea, and for the Arctic (Figure 8). For the Arctic Ocean regions including: the Kara, Laptev, East Siberian, Chukchi, Beaufort, central Arctic, and Canadian Arctic Archipelago, there is little change in the annual mean MO dates between the AHRA vs. AHRA-A and PMWC vs. PMWC-A data from year to year. The MO date time series curves for the original and adjusted data (Figures 7 and 8) do not overlap or cross for the Okhotsk, Bering, Hudson, Baffin, Greenland, Barents, and Kara regions indicating that the two algorithms are consistently detecting MO at different times during the spring. In seasonal ice regions where the ice is generally thinner, the influence of dynamic ice motion on SIC can more readily affect the passive microwave Tb signal; we expect greater uncertainty in MO date. We attribute the presence of offsets between the mean MO dates in the original and adjusted data to variation in algorithm sensitivity to spring weather events and to increased uncertainty of the algorithms in young, thin sea ice areas where a clear melting signal is harder to detect (as described in Section 3.1).

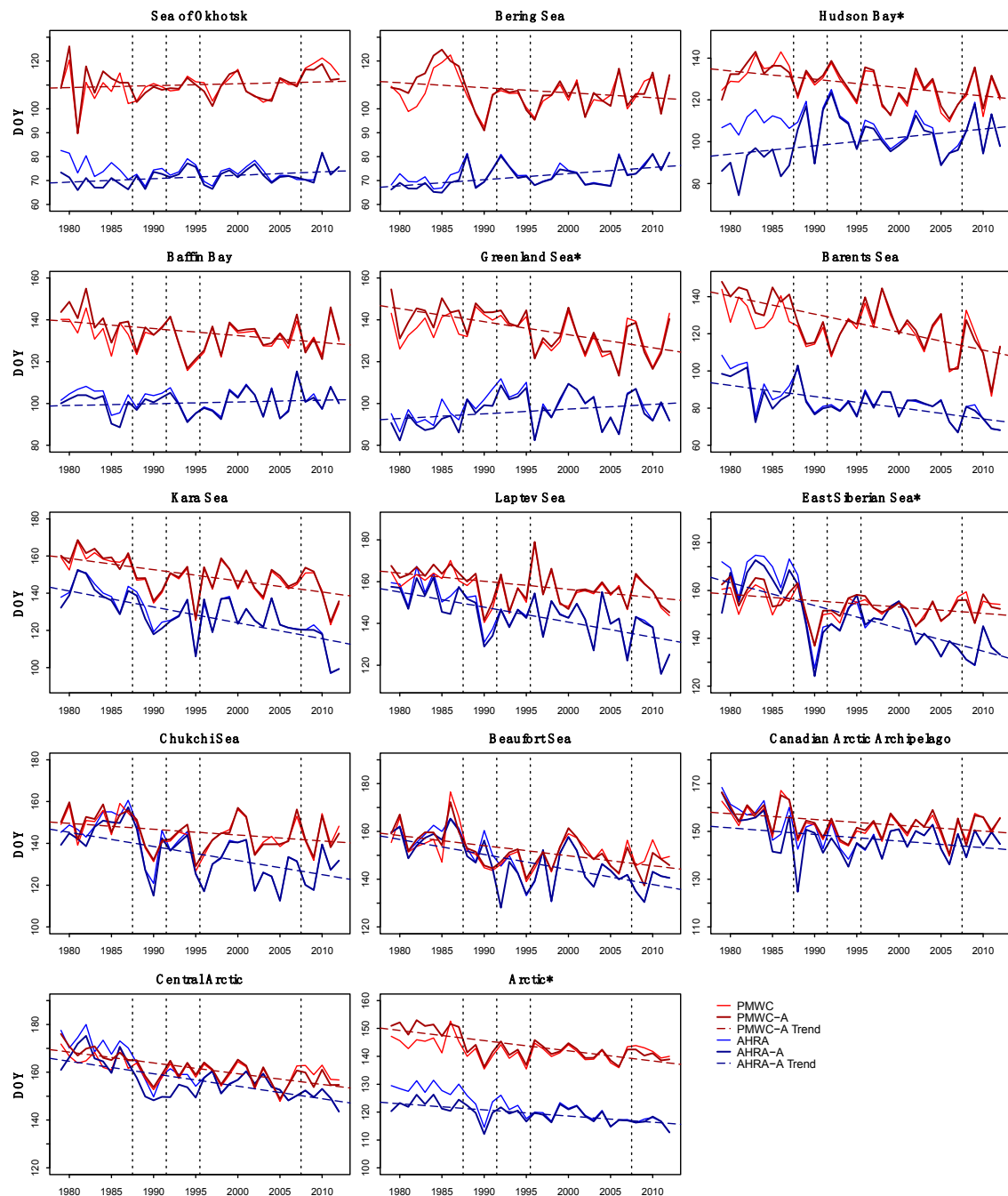


**Figure 8.** Annual mean MO date (DOY) for the AHRA-A and PMWC-A methods for 1979–2012. Least squares linear regression trends are shown as dashed lines. Original mean MO dates from the AHRA and PMWC methods (shown in Figure 7) are included here for comparison. Vertical dotted lines indicate when changes in passive microwave satellite sensors occur. Trends are significantly different at the 95% confidence level based on a Student's *t*-test in regions indicated with an asterisk.

While the average offsets between the original and adjusted MO dates increase slightly, the change in trend can be significant. When using PMWC-A data, the number of regions with statistically significant trends in mean MO date within the Arctic Ocean increases from three to eight (Table 3). The magnitude of the negative regional trends obtained with the PMWC-A is generally smaller than the AHRA-A trends (Table 3); however, the adjusted trends are now statistically significant for all regions except the Okhotsk and Bering Sea regions (Table 3). The statistically significant negative PMWC-A

trends for the Arctic Ocean regions are consistent with the AHRA-A negative trends. This strengthens the finding that a significant shift towards earlier MO has occurred over the 34-year study period for most of the sea ice regions and illustrates the effect of inter-sensor calibration effects on the time series of MO dates.

#### 4. Discussion

The results discussed in this work indicate some large differences between the two long records of early MO available for Arctic sea ice. Allowed to operate on identical Tb data, the algorithms produced statistically similar trends in MO date for much of the sea ice that were largely dissimilar in the original, unmodified datasets; however, the large differences in MO date produced by the two adjusted methods provide evidence of the algorithms differing sensitivity to day-to-day variability in Tbs. That is, the algorithms do not always detect melting on the same day and cannot be expected to identify identical MO dates in most regions of the Arctic. Our findings indicate that the AHRA generally indicates melting earlier and will be triggered by changes in the Tbs that the PMW method is insensitive to early in the year. In the marginal seas, a thin, young sea ice cover likely contributes to the larger offsets between mean MO time series observed. Dynamic thinning of the sea ice cover through divergence and resulting reductions in SIC could lead to an earlier melt signal in low spatial resolution passive microwave Tbs where the influence of sub-pixel scale features are present in the daily averaged Tbs. Thus increased short-term Tb variability from new ice forming in leads and open water within grid cells (e.g., [28]) could trigger MO in the algorithms while physical temperatures of the ice are still cold.

The agreement between MO methods is greatest in the central Arctic region; however, within this region, the spatial pattern of MO timing differs between the two methods as described in Section 3.2. The latest melting sea ice location in the PMWC MO date, north of the Kara and Barents Seas, contrasts with other measures for the timing of latest melting Arctic-wide. Wang et al. [21] compared PMW continuous MO for Arctic sea ice excluding the Canadian Arctic Archipelago region for 2000–2009 with simulated snowmelt runoff from the Canadian Coupled Global Climate Model. While runoff from melting is not equivalent to MO and would occur several days to weeks following the day of MO, the Wang et al. [21] results indicate that the latest melting region of the Arctic is more consistent with the AHRA location, north of Greenland and the Canadian Arctic Archipelago. Our results for the PMWC-A MO dates shown in Figure 5d indicate that corrected inter-sensor calibration of the adjusted MO dates reduced the magnitude of the extremely late MO dates present in the PMWC data north of the Kara Sea (Figure 5d). Overall, the PMWC-A mean MO dates are earlier than PMWC mean MO dates, however, the relative spatial pattern of the latest PMWC-A mean MO dates did not shift in location and remains similar to the original PMWC data (Figure 5a).

Based on a preliminary comparison, the AHRA, PMWC, and PMWC-A methods compare similarly to a new active microwave based MO detection method from RADARSAT-1 and RADARSAT-2 data in the northern Canadian Arctic Archipelago region developed by Mahmud et al. [19] (hereafter M16). The advantage of the M16 active method for MO detection is the higher spatial resolution (<100 m); however, image acquisition from the active microwave sensors in this region is limited to every 2–4 days [19] in contrast to daily observations (since late 1987) from the passive microwave sensors. Higher spatial resolution data are better able to resolve smaller scale variations in MO signatures in the land fast ice areas within the northern Canadian Arctic Archipelago where the relatively coarse resolution of the passive microwave data and effects of land contamination along coastlines make the passive microwave methods less reliable. The relatively lower frequency observations from the active microwave observations used by M16 are less sensitive to atmospheric effects, which contribute to increased uncertainty in passive microwave observations [28]. As shown in Figure 9, mean AHRA, PMWC, and PMWC-A MO dates calculated over the Canadian Arctic Archipelago region (Figure 1) north of latitude 75°N for the 1997–2012 period are an average of 7 days earlier than the M16 MO dates. The largest difference occurs in 2005 where the passive microwave MO dates are approximately

19 days earlier than the M16 MO date. We note that the altered AHRA-A data described in Section 2.5 are identical to the AHRA data for the 1997–2012 subset shown in Figure 9 and are omitted from the figure. The MO dates from the M16 method are expected to be later than the early MO dates from the AHRA and PMWC methods since the M16 data are produced from images during the early morning local time (i.e., when SAT is colder), thus are more comparable to the continuous MO date determined by the PMW, described further by Mahmud et al. [19]. The 2–4-day delay between images used by M16 could contribute to the later M16 MO dates. However, the mean difference of seven days between the M16 and the passive microwave MO dates is larger, indicating that other factors could also contribute to the differences such as the effects of the somewhat arbitrary selection of thresholds based on different Tb (for the AHRA and PMW) and backscatter (for M16) data. The higher spatial resolution MO dates compare reasonably well with both the AHRA and PMWC passive microwave MO timing, however, the limited spatial coverage and timeframe of the M16 MO dates prevent further comparison with the passive microwave methods discussed in this work.

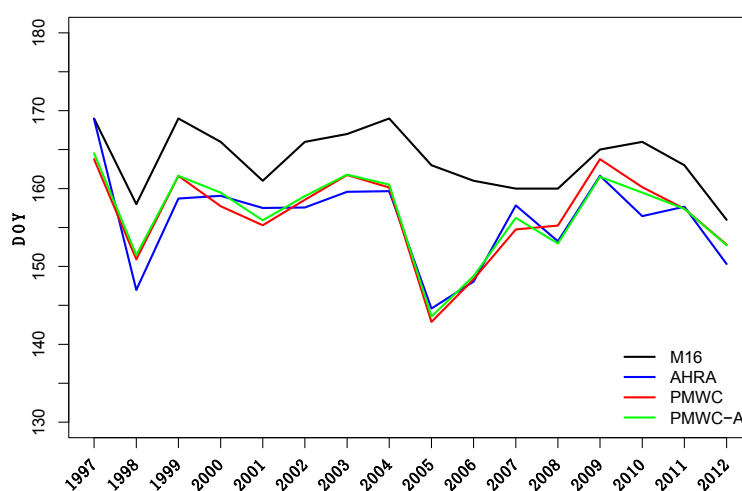


**Figure 9.** Mean MO dates for the Canadian Arctic Archipelago region (Figure 1) north of 75°N from the Mahmud et al. [19] RADARSAT method (M16) and the passive microwave AHRA, PMWC, and PMWC-A methods (1997–2012).

The passive microwave MO algorithms examined here have been unchanged since 2001 (AHRA) and 2009 (PMW). During the time since these algorithms were developed, the Arctic has continued its record breaking rapid reduction in sea ice extent and thickness [43–45]. Given that the two algorithms perform most inconsistently in regions with thin, more dynamic sea ice, and that the proportion of sea ice in the Arctic meeting this descriptive criteria is growing [46,47], the results presented here raise concern that the algorithms will perform poorly for a larger proportion of the Arctic without future adjustment. The changes in long-term trends in MO date for the PMWC and PMWC-A documented in this work further highlight the importance of careful application of inter-sensor calibration methods when long records of sea ice characteristics are examined.

## 5. Conclusions

This study assesses the similarity of MO dates from the AHRA and PMW, two long records of MO on Arctic sea ice derived from passive microwave observations for 1979–2012. Our results show large dissimilarities in the MO dates produced by the published versions of these two methods and disagreement in the long-term trend in MO timing over the 34-year record. The PMW method produces mean MO dates nearly three weeks later than the AHRA and shows smaller, statistically insignificant trends for most of the Arctic Ocean. By contrast, the AHRA MO dates indicate larger, statistically significant negative trends for all regions within the Arctic Ocean. The effects of procedural

differences between the two MO methodologies are documented and examined in this work by running the algorithms on identical source data and altering the masking and inter-sensor calibration methodologies to be the same. The adjusted MO data when compared to the original MO data indicate improved agreement of decadal trends, increasing confidence in the observed trend towards earlier MO for the Arctic over the satellite record. Interestingly, the average offsets between the adjusted AHRA and PMW increases by four days; however, the regional trends agree more closely and trends from the PMWC-A are statistically significant over the Arctic Ocean regions, more closely aligned with the AHRA-A MO trends.

While large differences in regional mean MO dates determined by each method were not improved in our adjusted data, it is clear that the largest differences between methods are restricted to thin ice regions of the Arctic. Examples shown indicate false MO detection when the melt parameters used by each method fall outside of predetermined thresholds within each algorithm. While this result is not unexpected, it is surprising to note the extent of sea ice regions for which this is the case. Given that sea ice in the Arctic is continuing to lose volume, the results of this work indicate the need for future improvements in algorithms of this type, which rely on threshold values to identify sea ice characteristics. The need for consistent inter-sensor calibration is evident when comparing the adjusted MO dates to the existing MO data due to the changes in decadal trends such that the magnitude of the trends is increased for some regions of the Arctic and statistical significance of the observed trends is increased over larger sea ice area. Thus, we have higher confidence in the trend towards increasingly early MO for most of the Arctic Ocean sea ice cover identified by Bliss and Anderson [23] and consistent with the shortened sea ice season reported by Parkinson [6], but not readily evident in the trends shown in Stroeve et al. [24] and Markus et al. [5]. We conclude that the results presented in this work indicate that caution should be used when interpreting results of both MO algorithms in first-year sea ice regions where uncertainty is greatest and note the sensitivity of long-term trends in sea ice characteristics to inter-sensor calibration methodology.

**Acknowledgments:** This work is has been funded by NASA master grant NNX12AD03A (task 718) awarded to ESSIC and NASA grant NNX16AK43G. The authors thank Mark R. Anderson for providing the AHRA v3 code used to for the comparison and sensitivity analysis. Three anonymous reviewers improved this work with their constructive feedback.

**Author Contributions:** A.B. performed the analysis and comparisons and prepared the manuscript, tables, and Figures 1 and 5, Figures 6–8. J.M. produced the adjusted data used in the sensitivity analysis, provided firsthand knowledge of the PMW algorithm, and provided Figures 2–4. W.M. contributed to the comparison methodology design and reviewed the paper prior to submission.

**Conflicts of Interest:** The authors declare no conflict of interest.

## References

1. Gloersen, P.; Campbell, W.J.; Cavalieri, D.J.; Comiso, J.C.; Parkinson, C.L.; Zwally, H.J. Satellite passive microwave observations and analysis of Arctic and Antarctic sea ice, 1978–1987. *Ann. Glaciol.* **1993**, *17*, 149–154. [[CrossRef](#)]
2. Comiso, J.C.; Parkinson, C.L.; Gersten, R.; Stock, L. Accelerated decline in the Arctic sea ice cover. *Geophys. Res. Lett.* **2008**, *35*, L01703. [[CrossRef](#)]
3. Cavalieri, D.J.; Parkinson, C.L. Arctic sea ice variability and trends, 1979–2010. *Cryosphere* **2012**, *6*, 881–889. [[CrossRef](#)]
4. Belchansky, G.I.; Douglas, D.C.; Platonov, N.G. Duration of the Arctic sea ice melt season: Regional and interannual variability, 1979–2001. *J. Clim.* **2004**, *17*, 67–80. [[CrossRef](#)]
5. Markus, T.; Stroeve, J.C.; Miller, J. Recent changes in Arctic sea ice melt onset, freezeup, and melt season length. *J. Geophys. Res. Oceans* **2009**, *114*, C12024. [[CrossRef](#)]
6. Parkinson, C.L. Spatially mapped reductions in the length of the Arctic sea ice season. *Geophys. Res. Lett.* **2014**, *41*, 4316–4322. [[CrossRef](#)] [[PubMed](#)]

7. Perovich, D.K.; Nghiem, S.V.; Markus, T.; Schweiger, A. Seasonal evolution and interannual variability of the local solar energy absorbed by the Arctic sea ice-ocean system. *J. Geophys. Res. Oceans* **2007**, *112*, C03005. [[CrossRef](#)]
8. Persson, P.O.G. Onset and end of the summer melt season over sea ice: Thermal structure and surface energy perspective from SHEBA. *Clim. Dyn.* **2012**, *39*, 1349–1371. [[CrossRef](#)]
9. Crane, R.G.; Anderson, M.R. Springtime microwave emissivity changes in the southern Kara Sea. *J. Geophys. Res. Oceans* **1994**, *99*, 14303–14309. [[CrossRef](#)]
10. Curry, J.A.; Schramm, J.L.; Ebert, E.E. Sea-ice albedo climate feedback mechanism. *J. Clim.* **1995**, *8*, 240–247. [[CrossRef](#)]
11. Drobot, S.D.; Anderson, M.R. Comparison of interannual snowmelt-onset dates with atmospheric conditions. *Ann. Glaciol.* **2001**, *33*, 79–84. [[CrossRef](#)]
12. Bliss, A.C.; Anderson, M.R. Daily area of snow melt onset on Arctic sea ice from passive microwave satellite observations 1979–2012. *Remote Sens.* **2014**, *6*, 11283–11314. [[CrossRef](#)]
13. Mortin, J.; Svensson, G.; Graversen, R.G.; Kapsch, M.-L.; Stroeve, J.C.; Boisvert, L.N. Arctic sea ice controlled by atmospheric moisture transport. *Geophys. Res. Lett.* **2016**, *43*, 6636–6642. [[CrossRef](#)]
14. Smith, D.M. Observation of perennial Arctic sea ice melt and freeze-up using passive microwave data. *J. Geophys. Res. Oceans* **1998**, *103*, 27753–27769. [[CrossRef](#)]
15. Drobot, S.D.; Anderson, M.R. An improved method for determining snowmelt onset dates over Arctic sea ice using Scanning Multichannel Microwave Radiometer and Special Sensor Microwave/Imager data. *J. Geophys. Res. Atmos.* **2001**, *106*, 24033–24049. [[CrossRef](#)]
16. Belchansky, G.I.; Douglas, D.C.; Mordvintsev, I.N.; Platonov, N.G. Estimating the time of melt onset and freeze onset over Arctic sea-ice area using active and passive microwave data. *Remote Sens. Environ.* **2004**, *92*, 21–39. [[CrossRef](#)]
17. Winebrenner, D.P.; Nelson, E.D.; Colony, R.; West, R.D. Observation of melt onset on multiyear Arctic sea ice using the ERS 1 synthetic aperture radar. *J. Geophys. Res.* **1994**, *99*, 22425–22441. [[CrossRef](#)]
18. Kwok, R.; Cunningham, G.F.; Nghiem, S.V. A study of the onset of melt over the Arctic ocean in RADARSAT synthetic aperture radar data. *J. Geophys. Res. Oceans* **2003**, *108*, 3363. [[CrossRef](#)]
19. Mahmud, M.S.; Howell, S.E.L.; Geldsetzer, T.; Yackel, J. Detection of melt onset over the northern Canadian Arctic Archipelago sea ice from RADARSAT, 1997–2014. *Remote Sens. Environ.* **2016**, *178*, 59–69. [[CrossRef](#)]
20. Forster, R.R.; Long, D.G.; Jezek, K.C.; Drobot, S.D.; Anderson, M.R. The onset of Arctic sea-ice snowmelt as detected with passive- and active-microwave remote sensing. *Ann. Glaciol.* **2001**, *33*, 85–93. [[CrossRef](#)]
21. Wang, L.; Wolken, G.J.; Sharp, M.J.; Howell, S.E.L.; Derksen, C.; Brown, R.D.; Markus, T.; Cole, J. Integrated pan-Arctic melt onset detection from satellite active and passive microwave measurements, 2000–2009. *J. Geophys. Res. Atmos.* **2011**, *116*, D22103. [[CrossRef](#)]
22. Wang, L.; Derksen, C.; Brown, R.; Markus, T. Recent changes in pan-arctic melt onset from satellite passive microwave measurements. *Geophys. Res. Lett.* **2013**, *40*, 522–528. [[CrossRef](#)]
23. Bliss, A.C.; Anderson, M.R. Arctic sea ice melt onset from passive microwave satellite data: 1979–2012. *Cryosphere* **2014**, *8*, 2089–2100. [[CrossRef](#)]
24. Stroeve, J.C.; Markus, T.; Boisvert, L.; Miller, J.; Barrett, A. Changes in Arctic melt season and implications for sea ice loss. *Geophys. Res. Lett.* **2014**, *41*, 1216–1225. [[CrossRef](#)]
25. NASA National Snow and Ice Data Center Distributed Active Archive Center. Documentation: Polar Stereographic Projection and Grid. Available online: [https://nsidc.org/data/polar-stereo/ps\\_grids.html](https://nsidc.org/data/polar-stereo/ps_grids.html) (accessed on 22 September 2016).
26. Gloersen, P. *Nimbus-7 SMMR Polar Gridded Radiances and Sea Ice Concentrations*; Version 1; NASA DAAC at the National Snow and Ice Data Center: Boulder, CO, USA, 2006.
27. Livingstone, C.E.; Singh, K.P.; Gray, A.L. Seasonal and regional variations of active/passive microwave signatures of sea ice. *IEEE Trans. Geosci. Remote Sens.* **1987**. [[CrossRef](#)]
28. Eppler, D.T.; Farmer, L.D.; Lohanick, A.W.; Anderson, M.R.; Cavalieri, D.J.; Comiso, J.; Gloersen, P.; Garrity, C.; Grenfell, T.C.; Hallikainen, M.; et al. Passive microwave signatures of sea ice. In *Microwave Remote Sensing of Sea Ice*; American Geophysical Union: Washington, DC, USA, 1992; pp. 47–71.
29. Anderson, M.R.; Drobot, S.D. Spatial and temporal variability in snowmelt onset over arctic sea ice. *Ann. Glaciol.* **2001**, *33*, 74–78. [[CrossRef](#)]

30. Cavalieri, D.J.; Gloersen, P.; Campbell, W.J. Determination of sea ice parameters with the NIMBUS 7 SMMR. *J. Geophys. Res. Atmos.* **1984**, *89*, 5355–5369. [[CrossRef](#)]
31. Markus, T.; Cavalieri, D.J. Snow depth distribution over sea ice in the Southern Ocean from satellite passive microwave data. In *Antarctic Sea Ice: Physical Processes, Interactions and Variability*; Jeffries, M.O., Ed.; American Geophysical Union: Washington, DC, USA, 1998; pp. 19–39.
32. Meier, W.; Fetterer, F.; Savoie, M.; Mallory, S.; Duerr, R.; Stroeve, J. *NOAA/NSIDC Climate Data Record of Passive Microwave Sea Ice Concentration; Version 2*; NASA DAAC at the National Snow and Ice Data Center: Boulder, CO, USA, 2013.
33. Peng, G.; Meier, W.N.; Scott, D.J.; Savoie, M.H. A long-term and reproducible passive microwave sea ice concentration data record for climate studies and monitoring. *Earth Syst. Sci. Data* **2013**, *5*, 311–318. [[CrossRef](#)]
34. Jezek, K.C.; Merry, C.; Cavalieri, D.; Grace, S.; Bedner, J.; Wilson, D.; Lampkin, D. *Comparison between SMMR and SSM/I Passive Microwave Data Collected over the Antarctic Ice Sheet*; BPRC Technical Report; Byrd Polar Research Center: Columbus, OH, USA, 1991.
35. Abdalati, W.; Steffen, K.; Otto, C.; Jezek, K.C. Comparison of brightness temperatures from SSMI instruments on the DMSP F8 and F11 satellites for Antarctica and the Greenland ice sheet. *Int. J. Remote Sens.* **1995**, *16*, 1223–1229. [[CrossRef](#)]
36. Stroeve, J.; Maslanik, J.; Xiaoming, L. An intercomparison of DMSP F11- and F13-derived sea ice products. *Remote Sens. Environ.* **1998**, *64*, 132–152. [[CrossRef](#)]
37. Cavalieri, D.J.; Parkinson, C.L.; Digirolamo, N.; Ivanoff, A. Intersensor calibration between F13 SSMI and F17 SSMIS for global sea ice data records. *IEEE Geosci. Remote Sens. Lett.* **2012**, *9*, 233–236. [[CrossRef](#)]
38. Maslanik, J.; Stroeve, J. *DMSP SSM/I-SSMIS Daily Polar Gridded Brightness Temperatures; Version 4*; NASA DAAC at the National Snow and Ice Data Center: Boulder, CO, USA, 2004.
39. Cavalieri, D.J.; Gloersen, P.; Zwally, H.J. *Near-Real-Time DMSP SSM/I-SSMIS Daily Polar Gridded Brightness Temperatures; Version 1*; Maslanik, J., Stroeve, J., Eds.; NASA DAAC at the National Snow and Ice Data Center: Boulder, CO, USA, 1999.
40. Rigor, I.G.; Colony, R.L.; Martin, S. Variations in surface air temperature observations in the Arctic. *J. Clim.* **2000**, *13*, 896–914. [[CrossRef](#)]
41. Anderson, M.R.; Bliss, A.C.; Drobot, S.D. *Snow Melt Onset over Arctic Sea Ice from SMMR and SSM/I-SSMIS Brightness Temperatures; Version 3*; NASA DAAC at the National Snow and Ice Data Center: Boulder, CO, USA, 2014.
42. Cavalieri, D.J.; Parkinson, C.L.; Gloersen, P.; Comiso, J.C.; Zwally, H.J. Deriving long-term time series of sea ice cover from satellite passive-microwave multisensor data sets. *J. Geophys. Res.* **1999**, *104*, 15803–15814. [[CrossRef](#)]
43. Kwok, R.; Cunningham, G.F.; Wensnahan, M.; Rigor, I.; Zwally, H.J.; Yi, D. Thinning and volume loss of the Arctic ocean sea ice cover: 2003–2008. *J. Geophys. Res. Oceans* **2009**, *114*, C07005. [[CrossRef](#)]
44. Parkinson, C.L.; di Girolamo, N.E. New visualizations highlight new information on the contrasting Arctic and Antarctic sea-ice trends since the late 1970s. *Remote Sens. Environ.* **2016**, *183*, 198–204. [[CrossRef](#)]
45. Comiso, J.C. Large decadal decline of the Arctic multiyear ice cover. *J. Clim.* **2012**, *25*, 1176–1193. [[CrossRef](#)]
46. Nghiem, S.V.; Rigor, I.G.; Perovich, D.K.; Clemente-Colón, P.; Weatherly, J.W.; Neumann, G. Rapid reduction of Arctic perennial sea ice. *Geophys. Res. Lett.* **2007**, *34*, L19504. [[CrossRef](#)]
47. Tschudi, M.; Fowler, C.; Maslanik, J.; Stroeve, J. Tracking the movement and changing surface characteristics of Arctic sea ice. *IEEE J. Sel. Top. Appl. Earth Obs. Remote Sens.* **2010**, *3*, 536–540. [[CrossRef](#)]

